A&A, 708, A384 (2026)
https://doi.org/10.1051/0004-6361/202658986

Astronomy & Astrophysics

Probing the Milky Way halo with RR Lyrae stars from *Gaia* Data Release 3

T. Muraveva[1,⋆], L. Monti[1], D. Massari[1], M. De Leo[2], A. Garofalo[1], G. Clementini[1], E. Ceccarelli[1,2], and U. Michelucci[3,4]

[1] INAF – Osservatorio di Astrofisica e Scienza dello Spazio di Bologna, via Piero Gobetti 93/3, Bologna 40129, Italy
[2] Dipartimento di Fisica e Astronomia-Universitá di Bologna, via Piero Gobetti 93/2, Bologna 40129, Italy
[3] Computer Science Department, Lucerne University of Applied Sciences and Arts, Luzern 6002, Switzerland
[4] TOELT LLC, Machine Learning Research and Development Department, Winterthur 8406, Zurich, Switzerland

Received 15 January 2026 / Accepted 19 February 2026

ABSTRACT

Context. The Milky Way (MW) stellar halo, containing debris from past accretion events, serves as a fossil record of hierarchical mass assembly. Due to their distinct properties, RR Lyrae stars (RRLs) serve as excellent tracers for identifying and characterising the halo's sub-structures. Thanks to the advent of *Gaia* Data Release 3 (DR3), which includes high-precision positions, parallaxes, proper motions, and radial velocities, along with the identification and characterisation of thousands of RRLs, it has become possible to study the distribution, kinematics, and metallicity of RRLs in the various dynamical sub-structures with unprecedented detail.
Aims. Our primary goal is to identify and characterise the dynamical sub-structures of the MW halo using RRLs from *Gaia* DR3.
Methods. We analysed a sample of 4933 RRLs, for which we calculated the integrals of motion and orbital parameters. We applied the domain-informed novelty detection CLustering in Multiphase Boundaries (CLiMB) framework to identify RRL membership in the MW sub-structures. We then used newly calibrated photometric metallicities available in the literature to study the metallicity distributions of RRLs in different sub-structures.
Results. We analysed the metallicity distributions of RRLs in major accreted system remnants as a snapshot of their chemical evolutionary status during early epochs. We calculated the weighted mean metallicity ([Fe/H]) and the corresponding standard deviation for *Gaia* Sausage/Enceladus ([Fe/H] = −1.57 ± 0.25 dex), Sequoia ([Fe/H] = −1.64 ± 0.26 dex), and the Helmi streams ([Fe/H] = −1.66 ± 0.19 dex). The metallicity distribution of RRLs in Thamnos was found to be bimodal, with the metal-poor peak likely representing the genuine (i.e. true) accreted Thamnos population ([Fe/H] = −1.94 ± 0.20 dex), in agreement with recent works based on spectroscopic abundances. Our analysis shows that the sub-structures ED-1 and L-RL3 are highly contaminated by thick-disc stars. However, the metal-poor tails in their metallicity distributions might be signatures of remnants from small accreted systems. We also identified some over-densities of RRLs in correspondence with the recently reported sub-structures Shiva and Shakti, which we suggest are of an in situ origin. Finally, we applied the RRL-based mass–metallicity relation of galaxies to test the nature of the identified dynamical sub-structures.

Key words. techniques: photometric – stars: abundances – stars: variables: RR Lyrae – Galaxy: halo

1. Introduction

The hierarchical mass assembly history of the Milky Way (MW) is a fundamental prediction of the Λ cold dark matter (ΛCDM) cosmological model, which posits that galaxies grow through successive mergers with smaller systems (White & Frenk 1991). Consequently, the MW's stellar halo is expected to be largely composed of debris from accreted dwarf galaxies and globular clusters (GCs), preserving a fossil record of these past interactions. Stars originating from the same disrupted progenitor are predicted to retain coherence in their integrals of motion (IoM) and to display characteristic chemical abundance patterns, even long after phase mixing has occurred (Johnston et al. 1996; Helmi & de Zeeuw 2000; Gómez et al. 2013; Helmi 2020). Identifying such stellar sub-structures in the Galactic halo provides powerful constraints on the formation and evolutionary history of the MW.

In recent years, numerous studies have identified sub-structures in the stellar halo that are believed to be remnants of past accretion events (e.g. Helmi et al. 1999; Koppelman et al. 2019a; Massari et al. 2019; Belokurov et al. 2018; Helmi et al. 2018; Myeong et al. 2019; Kruijssen et al. 2020; Naidu et al. 2020; Horta et al. 2021; Oria et al. 2022; Ruiz-Lara et al. 2022; Tenachi et al. 2022; Malhan & Rix 2024; Dodd et al. 2025a,b). However, interpreting these discoveries remains challenging. Numerical simulations show that debris from a single merger can generate multiple over-densities in different regions of IoM space, which could be mistakenly interpreted as distinct sub-structures (Koppelman et al. 2020; Amarante et al. 2022; Belokurov et al. 2023; Davies et al. 2023). Conversely, remnants of different progenitors can significantly overlap in IoM space (Helmi & de Zeeuw 2000; Naidu et al. 2020; Lövdal et al. 2022; Dodd et al. 2023), while contamination from unrelated sources can strongly affect kinematically selected samples of candidate members (Buder et al. 2022; Rey et al. 2023; Dodd et al. 2025b; Thomas et al. 2025). A promising approach to resolving these issues is to incorporate chemical abundance information, such as the metallicity ([Fe/H]) of stars associated with the sub-structures (Monty et al. 2020; Aguado et al. 2021; Matsuno et al. 2022; Horta et al. 2023; Ceccarelli et al. 2024; Mori et al. 2024).

⋆ Corresponding author: tatiana.muraveva@inaf.it

RR Lyrae stars (RRLs) are pulsating variable stars that serve as highly effective tracers of structures associated with past accretion events of the MW halo due to their distinct properties. They are numerous in the MW halo and easily recognisable thanks to their characteristic light curves and short pulsation periods (typically less than one day). Although recent studies suggest that relatively young and metal-rich RRLs can form through the evolution of close binary systems (Sarbadhicary et al. 2021; Bobrick et al. 2024), the majority of RRLs are old (age≥10 Gyr) and, thus, they can provide information on the properties of the various stellar systems before they were accreted by the MW. Moreover, RRLs are excellent distance indicators (e.g. Catelan et al. 2004) and their metallicity can be estimated from photometric parameters, such as the pulsation period and Fourier decomposition parameters of their light curves, without requiring spectroscopic data (e.g. Jurcsik & Kovacs 1996; Morgan et al. 2007). With the advent of *Gaia* Early Data Release 3 (EDR3; Gaia Collaboration 2021), and Data Release 3 (DR3; Gaia Collaboration 2023b), which include high-precision measurements of positions, parallaxes, and proper motions for almost two billion stars, as well as radial velocities for 33 million objects, along with the identification and characterisation of thousands of RRLs (Clementini et al. 2023), it has become possible to study the distribution, kinematics, and metallicity of RRLs in various dynamical sub-structures in unprecedented detail.

Numerous studies have used RRLs to investigate different sub-structures in the MW halo associated with past accretion events. Cabrera Garcia et al. (2024) analysed a sample of RRLs with photometric metallicities and distance estimates from Li et al. (2023), combined with proper motions and radial velocities from *Gaia* DR3 (Gaia Collaboration 2023b). They applied the HDBSCAN clustering algorithm to the IoM, identifying 97 sub-structures and exploring their associations with known components of the MW, such as *Gaia* Sausage/Enceladus (GSE; Belokurov et al. 2018; Helmi et al. 2018), the metal-weak thick disc, Helmi streams (Helmi et al. 1999), Sequoia (Myeong et al. 2019; Matsuno et al. 2019), Sagittarius stream (Ibata et al. 1994), and Wukong (Naidu et al. 2020). Kunder et al. (2024) analysed a sample of 80 RRLs from the BRAVA-RR survey (Kunder et al. 2016, 2020) and attributed a small fraction of them to the accreted GSE population, while the dominant fraction was associated with the in situ, metal-poor Galactic component Aurora (Belokurov & Kravtsov 2022), which formed before the Galaxy developed a coherently rotating disc. However, Kunder et al. (2024) did not rule out the possibility that a fraction of these stars originated from an ancient accretion event such as Kraken/Heracles (Massari et al. 2019; Kruijssen et al. 2020; Horta et al. 2021). D'Orazi et al. (2024) derived metallicities from high-resolution (HR) spectra for 78 RRLs observed by the GALactic Archaeology with HERMES (GALAH) survey (De Silva et al. 2015; Buder et al. 2021). They complemented this dataset with additional RRLs for which HR or low-resolution (LR) spectroscopic metallicities are available in the literature, resulting in an extended catalogue of 535 RRLs. These authors provided preliminary associations of the analysed RRLs with GSE, the Helmi streams, Sequoia, Sagittarius, and Thamnos (Koppelman et al. 2019a), then investigated the metallicity distributions of RRLs in these sub-structures. Most recently, Sun et al. (2025) identified Galactic sub-structures in 5D space using RRLs from *Gaia* DR3 (Gaia Collaboration 2023b). They combined the positions and proper motions from *Gaia* DR3 with photometric metallicities and distances from Li et al. (2023), identifying several sub-structures, including GSE, the Helmi streams, Sequoia, and Wukong.

In this paper, we analyse different dynamical sub-structures of the MW using IoM and photometric metallicities of RRLs from the *Gaia* DR3 catalogue, with three key differences compared to previous studies. Firstly, we adopted the new photometric metallicities from Muraveva et al. (2025), derived from period-Fourier parameters-metallicity relations calibrated by means of machine learning algorithms, using RRLs with accurately measured spectroscopic metallicities (Crestani et al. 2021; Gilligan et al. 2021; Liu et al. 2020). Secondly, to identify sub-structures, we applied a newly developed domain-informed novelty detection CLustering in Multiphase Boundaries (CLiMB, Monti et al. 2026) framework, designed for datasets containing both labelled and unlabelled components. This algorithm is particularly well-suited for RRL studies, as purely unsupervised methods often struggle to perform reliably with sparse, low-density samples such as RRLs. Finally, for the first time, we applied the newly derived mass-metallicity relation (MZR) for galaxies based on RRLs (Bellazzini et al. 2025) to test the nature of the identified dynamical sub-structures.

The paper is organised as follows. In Section 2, we describe the dataset used in this study. Section 3 outlines the clustering algorithm utilised to identify the dynamical sub-structures of the MW. In Section 4, we present the metallicity distribution of RRLs in the identified sub-structures, while Section 5 analyses their MZR. Finally, Section 6 provides the conclusions and final remarks.

2. Dataset

The *Gaia* DR3 includes a clean catalogue of 270 891 RRLs analysed by the Specific Object Study (SOS) pipeline for Cepheids and RRLs (SOS Cep&RRL; Clementini et al. 2023). This catalogue provides, among other parameters, periods, amplitudes, and mean magnitudes in the G, G_{BP}, and G_{RP} bands, as well as Fourier decomposition parameters of the G-band light curves. In Muraveva et al. (2025), we further cleaned the *Gaia* DR3 sample of RRLs by comparing it with the OGLE IV catalogues (Soszyński et al. 2014, 2019) and by analysing the distribution of RRLs on the Bailey diagram (G-band amplitude versus pulsation period). This procedure yielded a sample of 258 696 stars, which we consider bona fide RRLs. We then calibrated new empirical relations between the metallicity of RRLs, their pulsation periods, and Fourier decomposition parameters using machine learning methods, based on accurate spectroscopic metallicities from the literature (Crestani et al. 2021; Gilligan et al. 2021; Liu et al. 2020). As a result, we obtained photometric metallicity estimates for 134 769 RRLs from the cleaned *Gaia* DR3 sample (Muraveva et al. 2025).

For our analysis, we selected RRLs from the cleaned sample for which coordinates, radial velocities, and proper motions were available in the *Gaia* EDR3 (Gaia Collaboration 2021) and DR3 catalogues (Gaia Collaboration 2023b), while geometric distances were estimated from the *Gaia* EDR3 parallaxes using a Bayesian approach (Bailer-Jones et al. 2021). This selection yielded a sample of 4933 RRLs, which we used as the reference catalogue (Table A.1) in this study. We chose parallax-based distances instead of distances derived from the RRL fundamental relations, such as the luminosity-metallicity relation in the visual band (e.g. Clementini et al. 2003; Bono et al. 2003) or the near-to-mid-infrared period-luminosity-metallicity relations (e.g. Longmore et al. 1986; Sollima et al. 2008;

Muraveva et al. 2018), for our sample of 4933 RRLs to avoid introducing potential systematic biases from metallicity-dependent fundamental relations into the measurement of distances. This approach ensures that the method we used to assign RRLs to different dynamical sub-structures is independent of the metallicity of the individual RRLs, allowing for a robust analysis of metallicity distributions across the identified sub-structures. Additionally, since our sample is primarily limited by the availability of radial velocity measurements, rather than distance constraints, and the vast majority of RRLs in the reference sample have accurate parallax data (uncertainties <0.1 mas for 4925 stars out of 4933), measuring distances from parallaxes provides a reliable and straightforward option.

We calculated the Galactocentric Cartesian coordinates (X, Y, Z) for the RRLs in our sample using their positions and estimated distances. The Sun was assumed to lie on the X-axis of a right-handed coordinate system. In this system, the X-axis points from the Sun toward the Galactic centre, the Y-axis points toward Galactic longitude $l = 90°$, and the Z-axis points toward the North Galactic Pole ($b = 90°$). The distance of the Sun from the Galactic centre was assumed to be 8.122 kpc (GRAVITY Collaboration 2018).

We then computed the IoM, including the total energy (E), the angular momentum along the Z-axis (L_z), and the component of angular momentum perpendicular to L_z ($L_\perp$), as well as orbital parameters (e.g. apocentre, pericentre, and eccentricity) for 4933 RRLs in the sample. These computations were performed using the AGAMA software package (Vasiliev 2019) and adopting the MW potential from McMillan (2017). For each RRL, we ran 100 Monte Carlo simulations of the orbit, assuming Gaussian uncertainties in distance, proper motion, and radial velocity. The final values of the dynamical parameters were derived as the median of their distributions. In the following analysis, we use the IoM, Cartesian coordinates, and photometric metallicities of RRLs in the reference catalogue (Table A.1) to study the dynamical sub-structures of the MW.

3. Clustering analysis

Prior to the execution of the clustering analysis, we implemented a specific preprocessing routine to mitigate biases and ensure isotropic metric properties. First, to mitigate systematic biases related to the absolute scale of the E observable that could introduce artificial correlations, we centred the total energy distribution. Given the vector of E values across all RRLs (e), the mean background total energy level μ_e was subtracted from the original values ($e' = e - \mu_e$). This procedure effectively removes the mean background energy level while preserving local kinematic structures. Subsequently, given the heterogeneous ranges of the features (E, L_z, $L_\perp$), the dataset was standardised using Z-score normalisation (zero mean, unit variance) via `StandardScaler` from scikit-learn[1] to ensure isotropic distance calculations.

To investigate the dynamical structures in the MW traced by RRLs, we applied the CLiMB library[2] (Monti et al. 2026), which implements a novel domain-informed novelty detection clustering algorithm. CLiMB is a semi-supervised, two-phase clustering algorithm designed for datasets containing both labelled and unlabelled components. In the first phase (K-bound), the algorithm incorporates prior knowledge by considering RRLs previously associated with known MW sub-structures, as reported in the literature, identifying additional RRLs in the sample that are likely members of these structures. It performs constrained clustering using an adapted K-means approach, entirely redesigned with the inclusion of boundaries and utilising the Mahalanobis distance metric, which is a multivariate distance measure that considers the covariance among variables. The Mahalanobis metric is essential when identifying stellar sub-structures in the space of IoM. Unlike the Euclidean metric, which assumes spherical clusters, it properly accounts for correlations and differing scales between features. The accreted structures typically appear as elongated debris rather than globular distributions. By incorporating the covariance matrix, CLiMB defines ellipsoidal boundaries that follow the natural dynamical manifold of stellar streams.

CLiMB incorporates prior knowledge through initial centroid positions (e.g. from literature-identified RRLs associated with known MW sub-structures) and enforces strict density, distance, and radial constraints. To ensure reproducibility and robustness, the hyperparameters governing these constraints were optimised by maximising the adjusted Rand index (ARI), a clustering similarity metric that quantifies the agreement between the algorithm output and a reference classification while correcting for chance, calculated on the sub-set of known sub-structures. The density constraint filters out sparse points by requiring a minimum local density (`density_threshold` = 0.005), ensuring that only points within well-defined regions are considered for assignment. The distance constraint requires that points lie within a maximum radius of their nearest centroid (`distance_threshold` = 0.5). Finally, the radial constraint prevents centroids from drifting significantly from their initial, knowledge-guided positions (`radial_threshold` = 0.1 and `convergence tolerance` = 0.01), ensuring robust convergence and adherence to prior domain information.

The RRLs that have not been assigned during the K-bound step (i.e. those failing any of the aforementioned constraints) are passed to the second phase, namely, the so-called exploratory clustering step. Here, density-based methods (such as DBSCAN) are applied to discover new, potentially irregular clusters among these previously unassigned stars. Using the optimal parameters from the first stage, we optimised the exploratory parameters by minimising the Davies-Bouldin index (DBI), an internal clustering validation metric that measures the average separation between clusters relative to their internal dispersion (Davies & Bouldin 2009) on the clusters discovered within the unclassified data. This yielded an optimal configuration of $\epsilon = 0.190$ and $min\_samples = 24$. This allows CLiMB to identify previously unknown sub-structures within the remaining RRL sample, thereby combining the benefits of guided analysis with unsupervised discovery of additional stellar clusters.

Recently, Dodd et al. (2023, hereafter D23) analysed a sample of 193 831 nearby MW halo stars for which accurate parallaxes and radial velocities are available in *Gaia* DR3. Using a single-linkage clustering algorithm in IoM space (E, L_z, $L_\perp$), together with Mahalanobis distances and metallicities, D23 identified seven major groups and eleven smaller independent clusters, many of which were already known from the literature. We cross-matched our catalogue of RRLs, compiled as described in Section 2, with the sample of D23 and found 2009 stars in common. Among these, we selected 468 RRLs that, according to D23, belong to one of the eight large known groups or clusters: GSE, L-RL3, Thamnos, Helmi streams, Sequoia, ED-1, L-RL64, and ED-2. The second column of Table 1 lists the number of RRLs in each sub-structure as classified by D23, while the top panels of Figure 1 show their distribution in the E–L_z and L_z–$L_\perp$ planes.

[1] https://scikit-learn.org
[2] https://github.com/LorenzoMonti/CLiMB

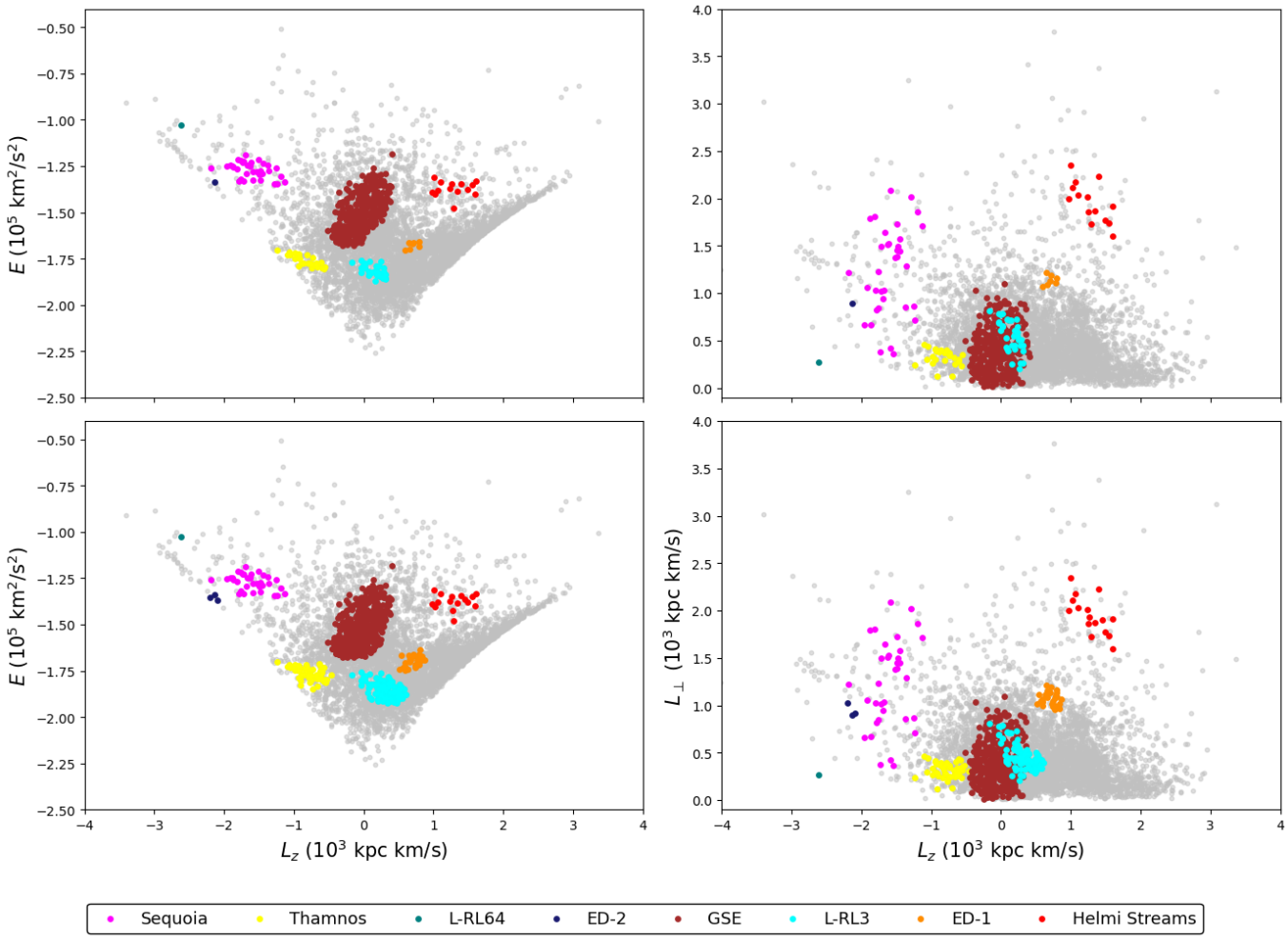

Fig. 1. Distribution of 4933 RRLs from our sample in the E–L_z and L_z–$L_\perp$ planes, colour-coded by the sub-structure to which they belong. Grey dots represent RRLs not assigned to any sub-structure. The top panels show RRLs identified in known sub-structures by cross-matching with D23, while the bottom panels display RRLs assigned to known sub-structures during the first phase of the CLiMB algorithm.

Table 1. RRLs in different MW sub-structures identified during the first phase of the CLiMB algorithm.

Substructure	N (D23)	N (CLiMB)	ΔN (%)
ED-1	7	27	286%
ED-2	1	3	200%
GSE	350	398	14%
Helmi streams	14	16	14%
L-RL3	34	102	200%
L-RL64	1	1	0%
Sequoia	35	35	0%
Thamnos	26	48	85%
Total	468	630	35%

Notes. Column 1: name of the sub-structure. Column 2: number of RRLs identified in the sub-structure by cross-matching with the D23 catalogue. Column 3: number of RRLs identified in the sub-structure using the CLiMB algorithm. Column 4: percentage increase in the number of RRLs identified in each sub-structure by the CLiMB algorithm compared to D23.

In the first phase of the CLiMB algorithm, all 468 RRLs are assigned the sub-structure labels of D23. These labelled stars serve as the initial training set for a semi-supervised clustering procedure, which then searches for additional members of the same sub-structures within the reference sample based on their distribution in IoM (E, L_z, $L_\perp$) space. Table 1 lists the number of stars in each sub-structure found by CLiMB, along with the percentage increase relative to the number of RRLs identified in each sub-structure by D23. The percentage increase ranges from 0% (no new RRLs identified) for L-RL64 and Sequoia, to 286% (the number of RRLs in the sub-structure increased by nearly four times) for ED-1. In total, 630 RRLs, shown in the bottom panels of Fig. 1, were assigned to known sub-structures by the CLiMB algorithm, 35% more than the 468 RRLs initially identified by D23.

In the second exploratory phase of the CLiMB algorithm, we removed the 630 RRLs identified as members of known sub-structures from the reference sample (Table A.1) and applied the DBSCAN algorithm with the optimised parameters described above to the remaining stars to search for new structures not reported by D23. This phase yielded three additional groups, shown in Table 2 and Fig. 2. The largest sub-structure, shown

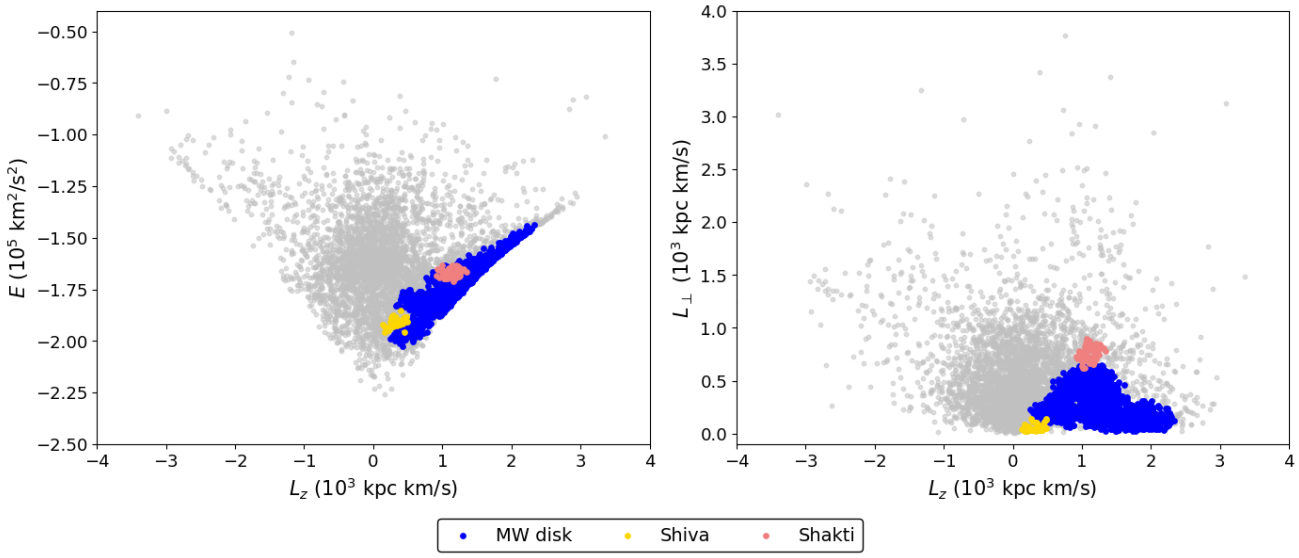

Fig. 2. Distribution of 4933 RRLs from our sample in the E–L_z and L_z–$L_\perp$ planes, colour-coded by the sub-structure to which they were assigned during the second phase of the CLiMB algorithm. Grey dots represent RRLs not assigned to any sub-structure.

Table 2. RRLs in different MW sub-structures identified during the second phase of the CLiMB algorithm.

Substructure	N
Disc CLiMB	1140
Shiva	38
Shakti	58
Total	1236

Notes. Column (1): name of the sub-structure. Column (2): number of RRLs identified in the sub-structure using the CLiMB algorithm.

in blue, occupies the region corresponding to the MW disc. The ability of CLiMB to recover the disc as an individual cluster supports the robustness of our method. However, the disc structure identified by CLiMB likely includes both the thin disc and the thick disc, as discussed further in Section 4.2. During the exploratory phase, we also identified two additional clusters, marked in pink and yellow in Fig. 2. In Section 4.10, we show that these clusters correspond to two newly reported sub-structures, Shiva and Shakti (Malhan & Rix 2024).

Overall, our semi-supervised, two-phase CLiMB algorithm enabled the identification of 1866 RRLs in 11 MW sub-structures, which are listed in Tables 1 and 2. The remaining 3067 RRLs from the reference sample were not assigned to any sub-structure. As a test, we removed RRLs identified in the 11 sub-structures and re-ran the exploratory phase of the CLiMB algorithm on the remaining sample of RRLs. No new clusters were identified. In the following section, we analyse in more detail the metallicity distribution of RRLs in the 11 sub-structures.

4. Metallicity distribution

4.1. Comparison with the literature

Metallicity values from Muraveva et al. (2025) are available for 4100 RRLs out of the 4933 in our sample. From these, we selected RRLs with metallicity uncertainties smaller than 0.5 dex, resulting in a final sample of 3614 RRLs, with a weighted mean metallicity and corresponding standard deviation of -1.47 ± 0.44 dex. Fig. 3 shows their distribution on the Cartesian Y-X and Z-X planes, colour-coded by metallicity.The third column of Table 3 reports the mean metallicity of RRLs assigned to each sub-structure identified in Section 3 using the CLiMB algorithm. As a consistency check, the fifth column provides the mean metallicities of RRLs assigned to each sub-structure solely through cross-matching with the D23 catalogue, excluding those added by CLiMB (Section 3). As shown, the metallicity values are generally in very good agreement (within 0.02 dex) for all but two sub-structures, confirming that the inclusion of new stars via CLiMB does not significantly affect the metallicity distribution of RRLs. This supports the robustness of our method. However, for two sub-structures (ED-2 and ED-1), the mean metallicity estimates differ by more than 0.15 dex, although they remain consistent within the uncertainties. We discuss these differences in more detail in Sections 4.7 and 4.8.

In Table 3, we also show the mean metallicity of RRLs in different sub-structures as reported in the literature (D'Orazi et al. 2024; Cabrera Garcia et al. 2024; Sun et al. 2025). We find that our mean metallicity values are in good agreement (within 0.1 dex) with the HR and LR spectroscopic metallicities reported by D'Orazi et al. (2024). In contrast, comparison of our estimates with the mean metallicities from Cabrera Garcia et al. (2024) and Sun et al. (2025) shows that our values are slightly more metal-rich, though still consistent within the uncertainties. Both of these studies adopt photometric metallicities from Li et al. (2023). As discussed in Muraveva et al. (2025) (see Section 4.1), the individual metallicities of first-overtone RRLs from Li et al. (2023) are systematically lower than those from Muraveva et al. (2025), most likely due to differences in the training sets used to calibrate the period–Fourier parameters–metallicity relations in the two studies. Therefore, the offset we observe between our mean metallicities and those reported by Cabrera Garcia et al. (2024) and Sun et al. (2025) can be attributed to the difference in the adopted metallicity scales. In the following sections, we analyse the metallicity distributions in the different sub-structures in more detail.

Table 3. Mean metallicities of RRLs in different sub-structures of the MW.

Substructure	*N* (CLiMB)	[Fe/H] (CLiMB) this study	*N* (D23)	[Fe/H] (D23) this study	[Fe/H] (D'Orazi et al. 2024)	[Fe/H] (Cabrera Garcia et al. 2024)	[Fe/H] (Sun et al. 2025)
Sequoia	29	−1.64 ± 0.26	29	−1.64 ± 0.26	−1.60 ± 0.33	−1.70 ± 0.26	−1.72 ± 0.32
Thamnos:	33	−1.76 ± 0.33	22	−1.75 ± 0.36	−1.75 ± 0.28 (*)	" "	" "
- Metal-rich component	10	−1.35 ± 0.12	" "	" "	" "	" "	" "
- Metal-poor component	23	−1.94 ± 0.20	" "	" "	" "	" "	" "
L-RL3	71	−1.54 ± 0.33	25	−1.56 ± 0.38	" "	" "	" "
L-RL64	1	−1.57 ± 0.41	1	−1.57 ± 0.41	" "	" "	" "
ED-2	2	−1.94 ± 0.32	1	−2.22 ± 0.34	" "	" "	" "
GSE	315	−1.57 ± 0.25	273	−1.56 ± 0.25	−1.65 ± 0.29	−1.61 ± 0.31	−1.62 ± 0.32
ED-1	18	−1.57 ± 0.40	6	−1.42 ± 0.28	" "	" "	" "
Helmi streams	12	−1.66 ± 0.19	10	−1.66 ± 0.19	−1.67 ± 0.29	−1.78 ± 0.33	−1.78 ± 0.30
Disc CLiMB:	838	−1.12 ± 0.48	" "	" "	" "	" "	" "
- Thin disc	238	−0.75 ± 0.40	" "	" "	" "	" "	" "
- Thick disc	600	−1.27 ± 0.42	" "	" "	" "	" "	" "
Shiva	30	−1.38 ± 0.29	" "	" "	" "	" "	" "
Shakti	40	−1.41 ± 0.38	" "	" "	" "	" "	" "

Notes. Column 1: name of the sub-structure. Column 2: number of RRLs in each sub-structure identified with the CLiMB algorithm, for which photometric metallicities from Muraveva et al. (2025) are available and have uncertainties smaller than 0.5 dex. Column 3: weighted mean metallicity of RRLs identified as belonging to the sub-structure using the CLiMB algorithm, with uncertainties calculated as the weighted standard deviation of the mean. For sub-structures containing only one star, the uncertainty corresponds to the photometric metallicity uncertainty of that individual star. Column 4: same as Column 2, but for RRLs identified as part of the sub-structure through cross-matching with the D23 catalogue. Column 5: same as Column 3, but for RRLs identified as part of the sub-structure through cross-matching with the D23 catalogue. Column 6: mean metallicity of RRLs from D'Orazi et al. (2024). Column 7: mean metallicity of RRLs from Cabrera Garcia et al. (2024). Column 8: mean metallicity of RRLs from Sun et al. (2025). (*) D'Orazi et al. (2024) provided the mean metallicities for Thamnos I and Thamnos II separately. In the table, we report the average of the two values.

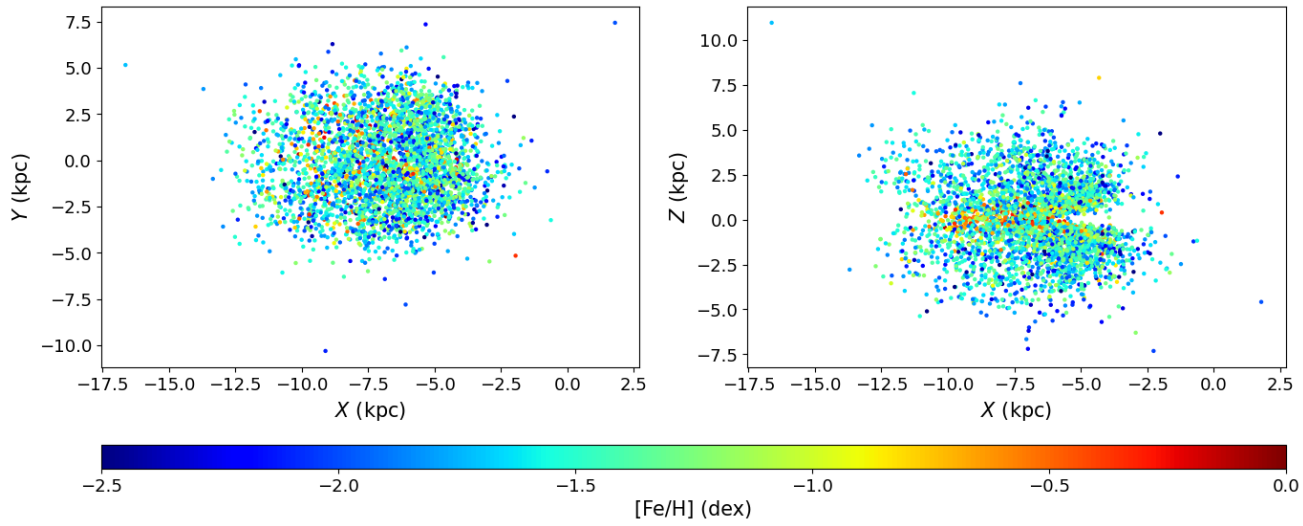

Fig. 3. Distribution of 3614 RRLs from the reference sample, for which the uncertainties in photometric metallicities are less than 0.5 dex, on the Cartesian *Y*–*X* (*left*) and *Z*–*X* (*right*) planes, colour-coded by metallicity.

4.2. MW disc

The thin disc is the dynamically cold component of the MW and the site of ongoing star formation (Helmi 2020). It was initially thought that the thin disc had been forming stars for 8–9 Gyr (Tononi et al. 2019). However, recent studies suggest that the thin disc may have formed less than 1 billion years after the Big Bang and has grown continuously since then, pushing back its onset by about 4–5 billion years compared to earlier estimates of 8–9 Gyr (Nepal et al. 2024). Kinematically, thin-disc stars are characterised by low eccentricities (*ecc*) and remain confined close to the Galactic plane, with a maximum vertical distance a star reaches above or below the Galactic plane during its orbit (Z_{max}) peaking at ∼0.36 kpc (Deepak 2024).

In contrast, the thick disc is a dynamically hotter and more vertically extended population (Helmi 2020), with a Z_{max} distribution peaking at ∼1.52 kpc (Deepak 2024). Analysis based on *Gaia* Data Release 2 (DR2, Gaia Collaboration 2018) supports the interpretation that the thick disc primarily formed during or after the merger with GSE (Gallart et al. 2019). Stars in the thick disc exhibit moderate eccentricities, peaking around 0.42, with most having $ecc < 0.8$ (Deepak 2024). The hot

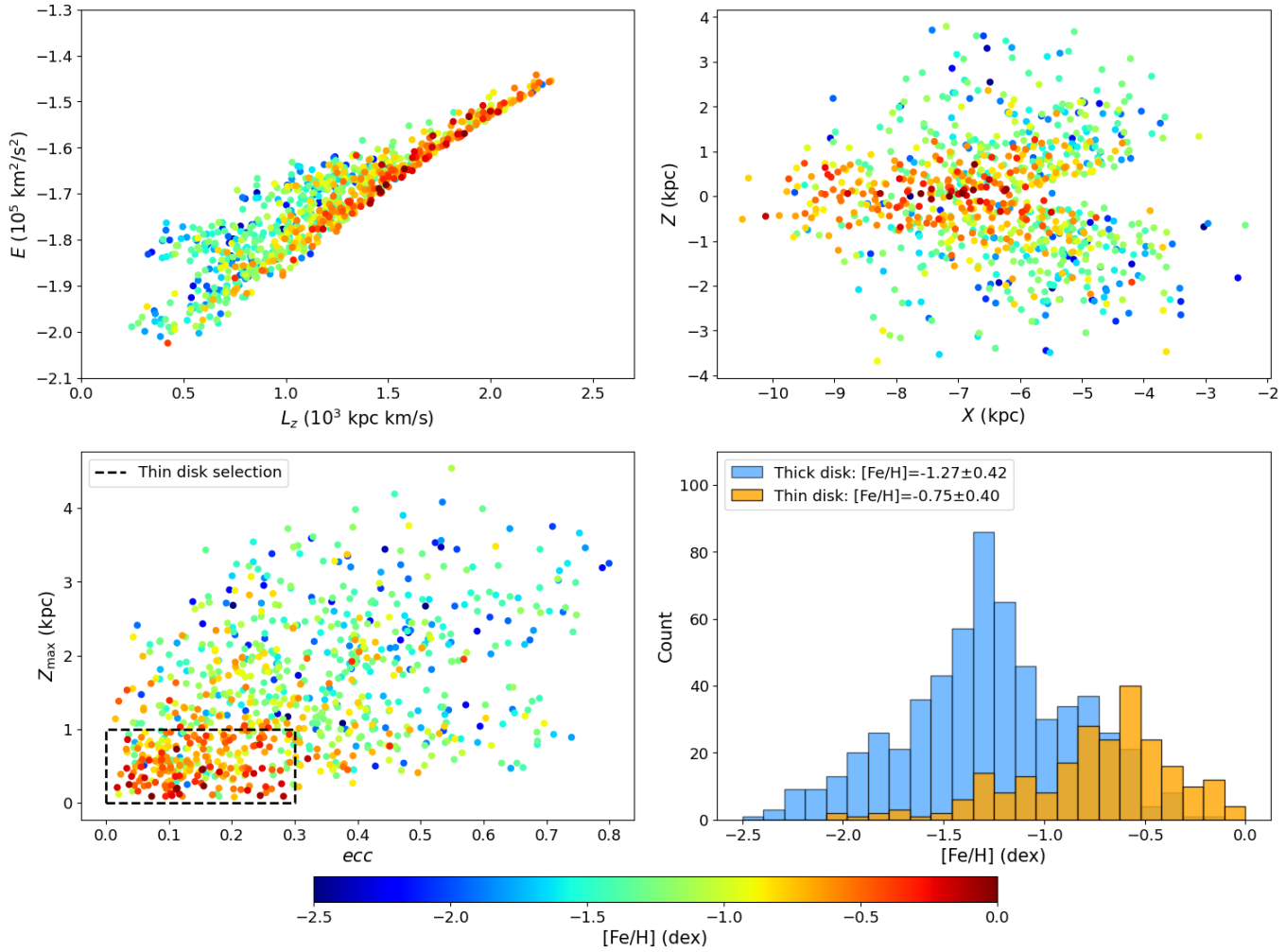

Fig. 4. Distribution of RRLs in the disc-like structure identified with the CLiMB algorithm in the E versus L_z (*top-left*), Cartesian Z versus X (*top-right*), and $Z_{\rm max}$ versus eccentricity (*bottom-left*) planes, colour-coded by metallicity. The black dashed line outlines the region used to select the thin-disc RRLs. Metallicity distributions of RRLs in the thin and thick discs, selected on the basis of their $Z_{\rm max}$ and eccentricity (*bottom-right*). See main text for details.

thick disc (HD), sometimes referred to as the Splash population (Di Matteo et al. 2019; Belokurov et al. 2020), consists of in situ disc stars dynamically heated by the GSE merger. Overall, HD stars exhibit hotter kinematics than the thick disc, with median eccentricities of $ecc \approx 0.35$ and a distribution notably skewed toward high-eccentricity stars, including a sub-set with $ecc = 0.5$–1.0 (Deepak 2024). Most HD stars are located within $Z_{\rm max} < 6$ kpc and the population has a median $Z_{\rm max}$ of 2.58 kpc (Deepak 2024).

It is noteworthy to mention that the picture provided to describe all these in situ components has recently encountered alternative scenarios. For example, it has been shown that clumpy star formation in the MW proto-disc can cause stars to be dynamically heated via clump instabilities, and to develop into a chemo-kinematically distinct thick disc (which would be coeval with the thin disc, see Beraldo e Silva et al. 2021). Such instabilities might also explain the emerging of a Splash-like population, without the need for a significant merger (Amarante et al. 2020).

During the exploratory phase of the CLiMB algorithm (Section 3), we identified an extended disc-like structure (blue dots in Fig. 2). It likely includes stars from both the thin and thick discs, and possibly a small fraction of the HD. Fig. 4 shows the distribution of RRLs in this disc-like structure, as identified by CLiMB, in the E versus L_z, Cartesian Z versus X, and $Z_{\rm max}$ versus ecc planes, colour-coded by metallicity. As expected, dynamically cold, more metal-rich RRLs have lower eccentricities and are concentrated near the Galactic plane ($|Z| < 1$ kpc), corresponding to the thin disc. In contrast, dynamically warm, more metal-poor RRLs exhibit a more extended spatial distribution ($|Z| < 4$ kpc) and have higher eccentricities, corresponding to the thick disc and likely including a small fraction of the HD.

Although a clear separation remains challenging, we made a tentative attempt to distinguish between the thin- and thick-disc RRL populations based on their orbital eccentricity and $Z_{\rm max}$. We adopt the criterion that RRLs with $ecc < 0.3$ and $Z_{\rm max} < 1$ kpc belong to the thin disc. The selected region is outlined by black dashed lines in the bottom-left panel of Fig. 4. RRLs located outside this region are likely members of the thick disc and HD. As we are unable to clearly disentangle the thick-disc and HD RRLs in our sample, we refer to this combined component simply as the 'thick disc' in the analysis described below. Accordingly, we divided the disc-like structure identified with CLiMB into two components: the thin disc, comprising 238 RRLs with a mean metallicity of [Fe/H] = -0.75 ± 0.40 dex, and the thick disc, comprising 600 RRLs with a mean metallicity of [Fe/H] = -1.27 ± 0.42 dex. The bottom-right panel of

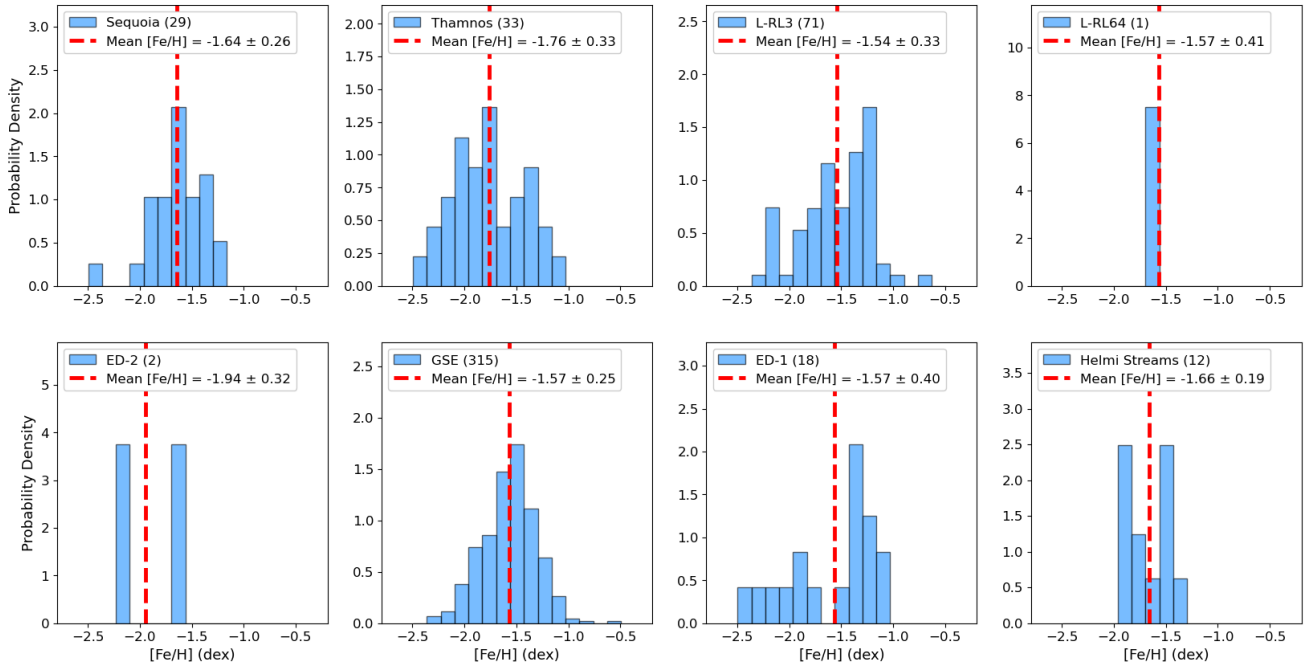

Fig. 5. Metallicity distribution of RRLs (light blue bins) in the known sub-structures of the MW halo. The dashed red line indicates the mean metallicity of RRLs in each sub-structure. Name of the sub-structure, number of RRLs with accurate metallicities, and mean metallicities are indicated in the legend. The uncertainties are calculated as the weighted standard deviation of the mean. For sub-structures containing only one star, the uncertainty corresponds to the photometric metallicity uncertainty of that individual star.

Fig. 4 presents the metallicity distributions of RRLs in the thin and thick discs. As expected, the metallicity distribution of the thin-disc RRLs is notably skewed toward higher [Fe/H] values.

4.3. GSE

The GSE population is the remnant of relatively massive galaxy that merged with the MW approximately 8–11 Gyr ago (Belokurov et al. 2018; Helmi et al. 2018). This merger is considered a milestone in Galactic history and is responsible for a large fraction of the inner stellar halo (Di Matteo et al. 2019; Gallart et al. 2019; Belokurov et al. 2020; Helmi 2020). One of the defining characteristics of the GSE population is the stars' highly eccentric orbits and slightly retrograde motion (Myeong et al. 2018; Koppelman et al. 2018; Haywood et al. 2018). Various estimates of the stellar mass of the GSE progenitor exist in the literature, ranging from 2.7×10^8 to a few$\times 10^9$ $M_\odot$ (e.g. Helmi et al. 2018; Vincenzo et al. 2019; Kruijssen et al. 2020; Naidu et al. 2020; Lane et al. 2023).

The CLiMB algorithm identified 398 RRLs in GSE, with accurate photometric metallicities from Muraveva et al. (2025) available for 315 of them. In Fig. 5, we show the metallicity distribution of RRLs in the GSE. The distribution appears approximately Gaussian, with a mean metallicity of [Fe/H] = -1.57 ± 0.25 dex. The metallicity of old stellar populations, such as RRLs (age> 10 Gyr), represents the chemical evolution state of the GSE progenitor at a very early epoch. On one side, the metallicity we derive is fully consistent with that reported by Ceccarelli et al. (2024), who focused on the very retrograde, high-energy sub-set of GSE stars, which is expected to be dominated by stars originating from the outer regions of the GSE progenitor, where star formation likely ceased earlier than in the inner regions (Koppelman et al. 2020; Skúladóttir et al. 2025). On the other side, the mean metallicity of RRLs in GSE structure is significantly lower than the mean photometric metallicities derived for GSE giant stars ([Fe/H] = −1.19 dex, Bellazzini et al. 2023) and also lower than the GSE metallicity derived from the Large Sky Area Multi-Object Fiber Spectroscopic Telescope (LAMOST; Cui et al. 2012) Low-Resolution Spectroscopic (LRS) Survey ([Fe/H] = −1.24 dex, D23). Such observed difference in mean metallicities between the RRLs found in this study and the overall stellar population of the GSE progenitor from the literature suggests that the GSE progenitor continued to form stars for an extended period after the formation epoch of the RRLs (see e.g. Gallart et al. 2019; González-Koda et al. 2025), until star formation was eventually halted by the structure's accretion onto the MW.

4.4. Thamnos

The Thamnos structure was discovered by Koppelman et al. (2019a) in the local retrograde halo using data from *Gaia* DR2 (Gaia Collaboration 2018), the extended Apache Point Observatory Galactic Evolution Experiment (APOGEE) DR14 (Abolfathi et al. 2018), the LAMOST (Cui et al. 2012), and the Radial Velocity Experiment (RAVE) DR5 (Kunder et al. 2017). Koppelman et al. (2019a) identified two over-densities in chemo-dynamical space (Thamnos 1 and Thamnos 2), which they attributed to a common progenitor with a mass of less than 5×10^6 $M_\odot$. Thamnos is thought to be the remnant of a small dwarf galaxy accreted at an early stage, when the MW was not yet massive, or possibly around the same time as the GSE event (Naidu et al. 2020). Naidu et al. (2020) analysed the metallicity distribution of stars in Thamnos using data from the Hectochelle in the Halo at High Resolution (H3) survey (Conroy et al. 2019), and found a strong peak at [Fe/H] = −1.9 dex, which they attributed to Thamnos, as well as a second peak at [Fe/H] ∼−1.2 dex, attributed to GSE contamination.

Using the MZR, Naidu et al. (2020) estimated a stellar mass of 2×10^6 $M_\odot$ for Thamnos, in good agreement with the earlier estimate by Koppelman et al. (2019a).

Similarly, Dodd et al. (2025b), by analysing the Thamnos metallicity distribution from LAMOST DR7 (Cui et al. 2012), found that Thamnos has a pronounced metal-poor tail around [Fe/H]∼−2 dex, which they attributed to the signature of a small dwarf galaxy. Dodd et al. (2025b) also reported a large peak in the metallicity distribution around [Fe/H]∼−1.4 dex, which they associated with a combination of GSE contamination and the ancient, in situ population of Aurora (Belokurov & Kravtsov 2022). Ceccarelli et al. (2025) estimated a contamination fraction for the Dodd et al. (2025b) sample of Thamnos of about 78% across the whole metallicity range, mostly coming from in situ stars. Mori et al. (2025) found the fractions of stars in Thamnos chemically compatible with GSE and the metal-poor disc to be 48% and 19%, respectively.

Using the CLiMB algorithm, we identified 48 RRLs in Thamnos. Fig. 5 shows the metallicity distribution for the 33 RRLs in Thamnos with accurate metallicity estimates. The distribution appears visually bimodal, in agreement with previous studies (Naidu et al. 2020; Dodd et al. 2025b). We modelled this bimodal metallicity distribution with a two-component Gaussian Mixture Model (GMM). This approach provides a practical, data-driven method to statistically decompose the observed distribution into two Gaussian components, each representing a distinct sub-population. The GMM fitting divides the Thamnos sample into a metal-poor (23 RRLs) and a metal-rich (10 RRLs) component. The corresponding mean metallicities are [Fe/H] = −1.94 ± 0.20 dex and [Fe/H] = −1.35 ± 0.12 dex, respectively[3]. We associate the metal-poor component with the 'true' Thamnos population, corresponding to the actual remnant of the accreted dwarf, and identified independently by Dodd et al. (2025b) using *Gaia* photometry and by Ceccarelli et al. (2025) using HR-spectroscopy. The metal-rich component is likely contamination from RRLs of GSE and in situ origin. Interestingly, the RRL number ratio between the two populations favours the 'true' Thamnos, whereas in all other studies the likely contaminating, more metal-rich component is dominant. RRLs may therefore be ideal tracers for selecting the 'true' Thamnos population.

4.5. Sequoia

Sequoia is a significant sub-structure in the local retrograde halo at higher energies (Myeong et al. 2019; Matsuno et al. 2019). Its true nature has been debated for some time, either as an independent merger event or as the most external population of GSE lost during its first pericentric passage around the MW (Koppelman et al. 2020). Chemical evidence supports its interpretation as a separate dwarf galaxy (Matsuno et al. 2022; Ceccarelli et al. 2024), having stellar mass estimates ranging from $M_\star \sim 10^7$ $M_\odot$ (Koppelman et al. 2019a; Helmi & de Zeeuw 2000) to $M_\star = (0.8 \pm 0.2) \times 10^8$ $M_\odot$ (Kruijssen et al. 2020).

We analysed 29 RRLs with accurate metallicities associated with Sequoia using the CLiMB algorithm. Their metallicity distribution function (MDF) is shown in Fig. 5. The mean metallicity of RRLs in Sequoia is [Fe/H] = −1.64 ± 0.26 dex. This value is in good agreement with the mean spectroscopic metallicities derived for the overall Sequoia stellar population from the LAMOST LRS survey ([Fe/H] = −1.56 dex, Dodd et al. 2023) and HR spectroscopic data obtained with the Very Large Telescope and the Large Binocular Telescope ([Fe/H] = −1.66 dex, Ceccarelli et al. 2024). As discussed in Section 4.3, a significant difference between the mean metallicities of RRLs and the overall stellar population in GSE could indicate that the GSE progenitor continued to form stars for an extended period after the epoch of RRL formation (>10 Gyr), before star formation was halted by the accretion of GSE by the MW. If we assume that the progenitors of GSE and Sequoia are two independent galaxies, the small difference between the mean metallicity of RRLs and the overall stellar population in Sequoia suggests that star formation in this galaxy stopped close to the epoch of RRL formation. This early cessation of star formation could be due to the accretion of Sequoia by the MW occurring before the MW accreted GSE. Alternatively, star formation could have stopped earlier due to the smaller mass of the Sequoia progenitor compared to GSE, leading to less efficient and shorter-lived star formation. If we assume instead that Sequoia and GSE originated from a single progenitor, their slight chemical difference ([Fe/H] of −1.57 dex for GSE versus −1.64 dex for Sequoia) could reflect an internal metallicity gradient of the progenitor galaxy. In this scenario, Sequoia represents the outer metal-poor envelope that was tidally stripped early during the merger. In contrast, the GSE component represents the progenitor core, which remained gas-rich and continued forming stars and becoming further enriched until final accretion.

4.6. Helmi streams

The Helmi streams were among the first bona fide accreted sub-structures discovered in the MW halo via dynamical analysis (Helmi et al. 1999). Subsequently, Koppelman et al. (2019a,b) provided an updated view of these streams using *Gaia* DR2 data. The Helmi streams are interpreted as the debris of a disrupted dwarf galaxy, with the time of accretion estimated to be 5–8 Gyr ago (Kepley et al. 2007; Koppelman et al. 2019b). The stellar mass of the progenitor estimated in the literature is in the range $M_\star = (0.5\text{–}1) \times 10^8 M_\odot$ (e.g. Koppelman et al. 2019b; Naidu et al. 2020; Kruijssen et al. 2020).

Bellazzini et al. (2023) found that the Helmi streams have a metallicity distribution characterised by a median of −1.52 dex, with the 16th and 84th percentiles at −1.87 dex and −1.21 dex, respectively. The MDF of the 12 RRLs in the Helmi streams identified by the CLiMB algorithm is shown in Fig. 5. Their metallicities span a range from –1.90 to –1.42 dex, with a mean of [Fe/H] = −1.66 ± 0.19 dex, which is in good agreement with the value reported by Bellazzini et al. (2023). As in the case of Sequoia (Section 4.5), this could indicate that star formation in the Helmi streams progenitor stopped close to the epoch of RRL formation.

4.7. ED-1/L-RL3

ED-1 is a newly identified dynamical group discovered by D23. The MDF of ED-1, as studied by D23, spans a broad range and exhibits multiple peaks, approximately corresponding to the HD, GSE, and a more metal-poor component at [Fe/H] ∼−1.8 dex. D23 suggested that ED-1 includes contamination from both the HD and GSE, but the presence of a low-metallicity peak in its MDF, together with the chemical abundances of some of its stars, points toward an accreted origin for at least part of this sub-structure.

L-RL3 is a prominent sub-structure in the local stellar halo of the MW, located at low energy in IoM space. It was first

[3] Mean metallicities derived directly from the two-component GMM fitted to the [Fe/H] distribution for metal-poor and metal-rich components are −1.94 ± 0.21 and −1.36 ± 0.11 dex, respectively.

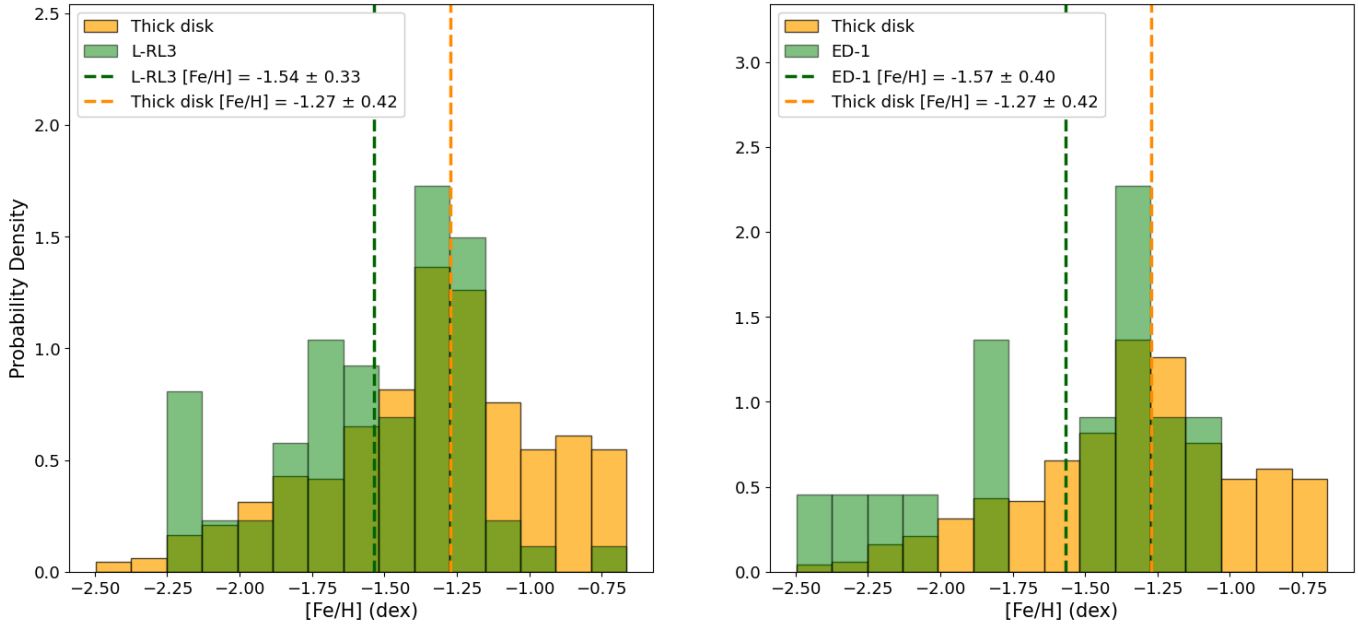

Fig. 6. Metallicity distribution of RRLs in L-RL3 (*left*) and ED-1 (*right*) shown in green bins. For comparison, the metallicity distribution of thick-disc RRLs, defined in Section 4.2, is shown in orange bins. Dashed green and orange lines indicate the mean metallicities of the sub-structures and the thick disc, respectively.

identified by Lövdal et al. (2022) and Ruiz-Lara et al. (2022), and later further characterised by D23. Its MDF reveals two main components: a high-metallicity population similar to that of the HD, and a well-populated low-metallicity tail. D23 suggested that L-RL3 comprises both in situ and accreted stars.

Accurate metallicities are available for 71 RRLs in L-RL3 and 18 RRLs in ED-1, with mean values of [Fe/H] = −1.54 ± 0.33 dex and [Fe/H] = −1.57 ± 0.40 dex, respectively. Both sub-structures are relatively metal-rich and located close to the thick disc in IoM space (Fig. 1), which could indicate that they are heavily contaminated by stars of the thick disc and the HD. In Fig. 6, we show the metallicity distributions of RRLs in L-RL3 (left panel) and ED-1 (right panel). For comparison, we also plot the metallicity distribution of RRLs in the thick disc, as defined by their eccentricity and $Z_{\max}$ (Section 4.2). The distributions appear visually similar, with closely positioned peak metallicities. The MDFs of both sub-structures also exhibit weak metal-poor tails, which may be remnants of small accreted systems. We performed a two-sample Kolmogorov–Smirnov (KS) tests to evaluate the hypothesis that L-RL3 and ED-1 are drawn from the same distribution as the thick-disc RRLs. The resulting p-values are 7.2×10^{-6} and 3.0×10^{-2} for L-RL3 and ED-1, respectively. These results indicate that L-RL3 and ED-1 are statistically inconsistent with being drawn from the thick-disc RRL distribution.

It is worth noting that (as mentioned in Section 4.1) there is a difference of more than 0.1 dex between the mean metallicities of RRLs in ED-1 identified by cross-match with D23 and those identified using the CLiMB algorithm. Moreover, the CLiMB algorithm added 286% more RRLs to ED-1 (see Table 1), compared with RRLs assigned to this sub-structure by D23. For a sanity check, we performed a two-sample KS test between the thick-disc RRLs and RRLs classified as belonging to ED-1 only by D23. The resulting p-values is 4.2×10^{-1}, indicating no statistically significant difference between the two distributions. This suggests that the ED-1 sample from D23 is consistent with being drawn from the thick-disc population. We caution that robust conclusions on the origin of ED-1 and L-RL3 cannot be drawn due to small sample sizes and the sensitivity of KS tests to the sample selection method. Still, the overlap in IoM space and metallicity distributions indicates that both sub-structures likely contain significant contamination from thick-disc stars, while the weak metal-poor tails in their MDFs may be signatures of remnants from small accreted systems.

4.8. ED-2

Recently, D23, using *Gaia* DR3 data, discovered a new structure ED-2 in the retrograde halo within the region associated with Sequoia in IoM space. Dodd et al. (2025a) found that stars in ED-2 are very metal-poor (mean [Fe/H] = −2.43 dex) and exhibit a small intrinsic metallicity dispersion (σ = 0.13 dex), in agreement with previous studies (Balbinot et al. 2024; Ceccarelli et al. 2024). They also estimated the age of ED-2 to be comparable to the age of the Universe, consistent with Balbinot et al. (2024). The progenitor of ED-2 is likely an ancient star cluster (Balbinot et al. 2024; Dodd et al. 2025a).

The CLiMB algorithm identified three RRLs in ED-2. Accurate metallicity estimates were available for only two of them, with values of [Fe/H] = −2.21 ± 0.34 dex and [Fe/H] = −1.57 ± 0.39 dex, resulting in a mean metallicity of [Fe/H] = −1.94 ± 0.32 dex for ED-2. Fig. 5 shows the metallicity distribution of RRLs in ED-2. The observed spread in metallicities, which differs from values reported in the literature, could be due to contamination of the ED-2 RRL sample by a more metal-rich star that is of an in situ or GSE origin. Indeed, as shown in Table 1, only one star with [Fe/H] = −2.21 ± 0.34 dex was classified as belonging to ED-2 based on a cross-match with the D23 catalogue. We can thus conclude that the additional metal-rich star identified in ED-2 by the CLiMB algorithm may not be a true member of the sub-structure and is likely a contaminant. In this case, the metallicity of the single confirmed ED-2 star would be consistent with literature values, supporting the interpretation of

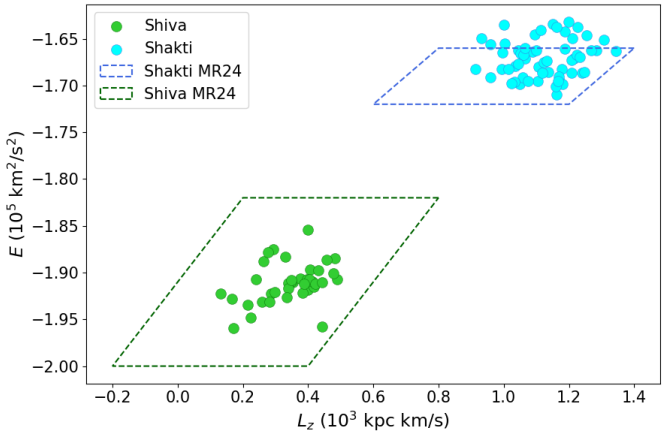

Fig. 7. RRLs in Shiva (green dots) and Shakti (cyan dots) identified by the CLiMB algorithm. Dashed green and blue lines outline the regions used by Malhan & Rix (2024, MR24) to identify members of Shiva and Shakti, respectively.

ED-2 as an extremely metal-poor structure, possibly the remnant of a GC.

4.9. L-RL64/Antaeus

L-RL64 is a newly discovered cluster located in the most retrograde region of IoM space (Lövdal et al. 2022; Ruiz-Lara et al. 2022). Subsequently, Oria et al. (2022) independently identified this sub-structure, naming it Antaeus. L-RL64 was initially thought to be the extreme retrograde tail of the Sequoia merger event, but it is now considered an independent accretion event, unrelated to Sequoia (Oria et al. 2022; Ruiz-Lara et al. 2022; Dodd et al. 2023; Ceccarelli et al. 2024).

Only one RRL from our sample with [Fe/H] = −1.57 ± 0.41 dex was identified as belonging to L-RL64, both by the CLiMB algorithm and via cross-matching with the D23 catalogue. Given its large uncertainty, the metallicity of this star is consistent with the distribution observed for L-RL64, as found by Ceccarelli et al. (2024), which peaks at [Fe/H] = −1.83 dex with a dispersion of 0.27 dex. However, we cannot exclude the possibility that the only RRL star identified in L-RL64 is a contaminant of in situ or GSE origin.

4.10. Shiva and Shakti

With the explorative phase of the CLiMB algorithm, we identified two sub-structures not included in the D23 catalogue, located near the MW disc (yellow and pink dots in Fig. 2). Recently, Malhan & Rix (2024) reported the discovery of two new sub-structures in the MW halo, named Shiva and Shakti. In Fig. 7, we show the positions of RRLs in our newly identified sub-structures on the E–L_z plane in correspondence to the area used to outline members of Shiva and Shakti by Malhan & Rix (2024), who also adopted the MW potential of McMillan (2017). As can be seen, there is significant overlap. We therefore conclude that the two sub-structures identified by the CLiMB algorithm correspond to Shiva and Shakti discovered by Malhan & Rix (2024), although we cannot be entirely certain, given that our sample of 4933 RRLs is significantly smaller than the sample of stars from *Gaia* DR3 used by Malhan & Rix (2024) to identify these over-densities (5 799 724 stars).

Malhan & Rix (2024) analysed various hypotheses regarding the origin of these two sub-structures. They found that both exhibit orbit-space distributions indicative of an accreted origin, yet their chemical abundance patterns are more typical of an in situ population. Malhan & Rix (2024) proposed two possible scenarios. In the first, these prograde sub-structures may have formed through resonant orbit trapping of field stars by the rotating Galactic bar. This interpretation is consistent with the findings of Dillamore et al. (2023), who identified a prominent ridge feature in phase space at constant energy and positive L_z, likely originating from stars trapped in corotation resonances with the MW's bar. Dillamore et al. (2023) showed that this ridge contains both metal-rich and metal-poor stars, with orbits lying between typical disc-like and halo-like trajectories. Malhan & Rix (2024) noted that Shakti is located near the tip of this ridge in the E–L_z plane, suggesting that it could have a resonant origin. In the second scenario, proposed by Malhan & Rix (2024), Shiva and Shakti are interpreted as protogalactic fragments that underwent rapid star formation and merged early in the Galaxy's history, similar to the building blocks of the MW's ancient inner regions.

The CLiMB algorithm identified 58 RRLs as belonging to Shakti, of which 40 have accurate metallicity measurements. Their metallicity distribution is shown in the right panel of Fig. 8, compared to the metallicity distribution of the thick disc, as defined in Section 4.2. As shown, the two distributions are visually similar. According to a KS test, the probability that our RRL samples of Shakti and the thick disc are drawn from the same metallicity distribution is not negligible ($p = 0.16$).

To investigate the hypothesis of a resonant origin for the over-density identified as Shakti, we implemented the approach of De Leo et al. (2026) to check whether any Shakti members were trapped in resonant orbits. Briefly, taking the presence and influence of the rotating bar of the MW fully into account, De Leo et al. (2026) developed an empirical method to identify resonant loci in dynamical parameter spaces. Analysing the large sample of stars from Bellazzini et al. (2023) composed of giants from the *Gaia* Synthetic Photometry Catalogue (Gaia Collaboration 2023a), the loci appear as clear over-densities in the periocentric radius–eccentricity space and in the space of 'characteristic' energy (E_{cha}) and angular momentum ($L_{z,cha}$). These characteristic values are defined as the mean of the corresponding IoM across the entire orbit integration (Moreno et al. 2015, 2021). Stars located close to or on top of the resonant loci in both dynamical spaces are considered trapped by resonances induced by the rotating bar. Fig. 9 shows the RRLs of Shakti (cyan points) in $L_{z,cha}$–E_{cha} space, over-plotted on the distribution of stars from Bellazzini et al. (2023) used to identify the resonant loci, which are highlighted with the red lines. As can be seen, Shakti lies precisely along the resonant loci in the $L_{z,cha}$–E_{cha} plane. We found that 14 out of 58 RRLs in Shakti (24%) are potentially trapped in resonant orbits, as evidenced by the cyan points clustered around $E_{cha} \approx -1.3 \times 10^5$ km^2/s^2 and $L_{z,cha} \approx 10^3$ kpc km/s. Based on Shakti's location in the $L_{z,cha}$–E_{cha} plane, the metallicity distribution of its RRLs, which is similar to that of the thick disc, and the significant fraction of stars held in resonant orbits, we conclude that the sub-structure corresponding to Shakti is likely part of the thick-disc population that became trapped in a ridge-like feature due to resonances with the MW bar.

Regarding the Shiva sub-structure, we identified 38 RRLs within it using the CLiMB algorithm. Photometric metallicity estimates are available for 30 of them, yielding a mean metallicity of [Fe/H] = −1.38 ± 0.29 dex. Their MDF is shown in the left panel of Fig. 8. Curiously, we found that 23 of the 38 RRLs discovered in correspondence with Shiva by CLiMB are members of the GC NGC 6121 (M4). To identify RRLs

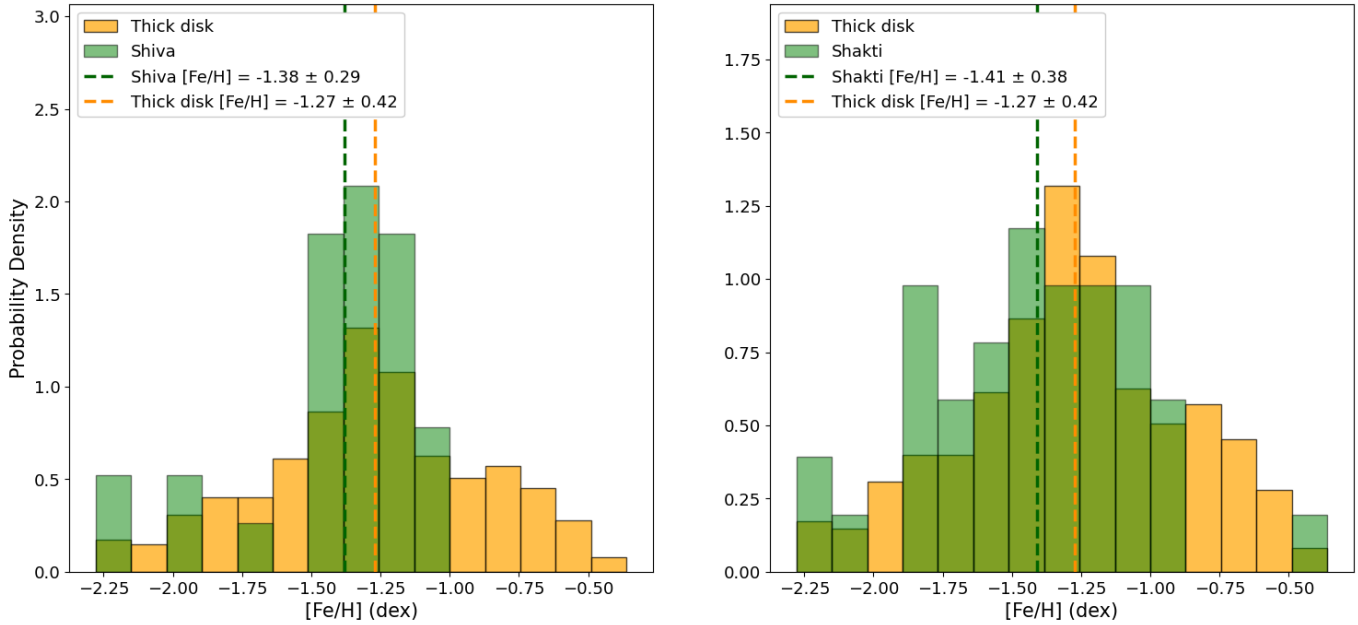

Fig. 8. Metallicity distribution of RRLs in Shiva (*left*) and Shakti (*right*) shown in green bins. For comparison, the metallicity distribution of thick-disc RRLs, defined in Section 4.2, is shown in orange bins. Dashed green and orange lines indicate the mean metallicities of the sub-structures and the thick disc, respectively.

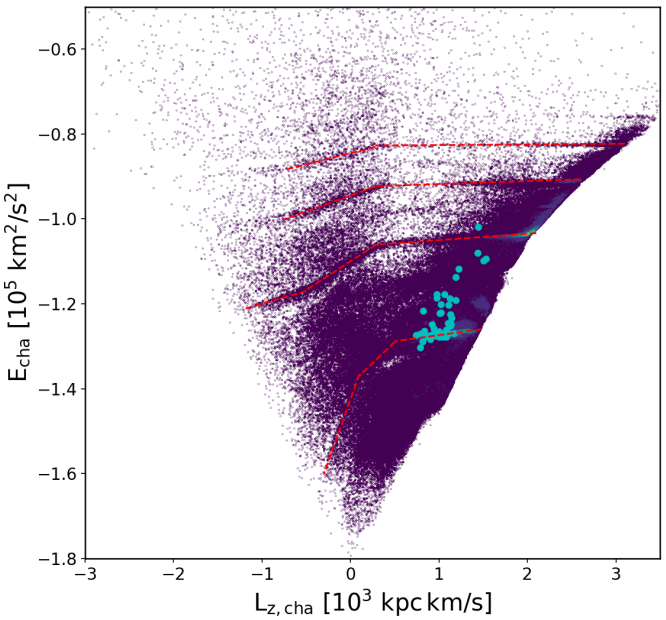

Fig. 9. Distribution of stars from Bellazzini et al. (2023) used to identify the resonant loci on the characteristic energy versus angular momentum plane (purple dots). Cyan points represent RRLs identified in Shakti by CLiMB, while red dashed lines indicate the resonance loci.

associated with NGC 6121, we used the catalogue by Clement et al. (2001)[4], which is continuously updated based on the literature and summarises the numbers and types of variable stars in various GCs. Fig. 10 shows the RRLs identified by CLiMB as part of Shiva (green dots), with the RRLs associated with NGC 6121 over-plotted (orange open circles). The black cross indicates the Cartesian coordinates of the centre of the NGC 6121 cluster, calculated as described in Section 2, using the coordinates from Baumgardt et al. (2019) and the distance to NGC 6121 as determined by Baumgardt & Vasiliev (2021). The discovery of Shiva by Malhan & Rix (2024) came after excluding the stars lying within five tidal radii of the GCs from the analysed sample. The Shiva over-density should therefore not coincide with NGC 6121. However, we cannot exclude that the stellar stream of NGC 6121, and especially the stars that have been lost recently by the GCs, might have contributed in enhancing the signal of such a dynamical over-density. It would be interesting to check this possibility by looking for the chemical signatures of GCs in the light element abundances of Shiva members.

[4] https://www.astro.utoronto.ca/~cclement/cat/listngc.html

5. Mass–metallicity relation

The MZR, the correlation between a galaxy's stellar mass and its metallicity, is a fundamental law of galaxies. The MZR has been observed to evolve with cosmic time. In Bellazzini et al. (2025), we demonstrated that the metallicity distributions of RRLs can be used to investigate the MZR of galaxies at early epochs ($z \gtrsim 3$), close to when the progenitors of present-day dynamical sub-structures merged into the MW. To construct the MZR in Bellazzini et al. (2025), we used the mean photometric metallicities of RRLs from Muraveva et al. (2025) in 14 dwarf galaxies and the MW, while stellar masses were taken from Pace (2025).

In Fig. 11, we plot the mean metallicity versus stellar mass for 14 dwarf galaxies (green circles) and the MW (blue star) from Bellazzini et al. (2025), as well as the known dynamical sub-structures analysed in this study (red squares): GSE, Sequoia, and the Helmi streams, for which stellar masses were determined by Kruijssen et al. (2020). The stellar masses were estimated by means of the neural network using the ages, metallicities, and orbital properties of GCs associated with the same progenitor galaxy. As can be seen, all analysed dynamical sub-structures lie within 2σ of the best-fit relation based on the 14 dwarf satellites

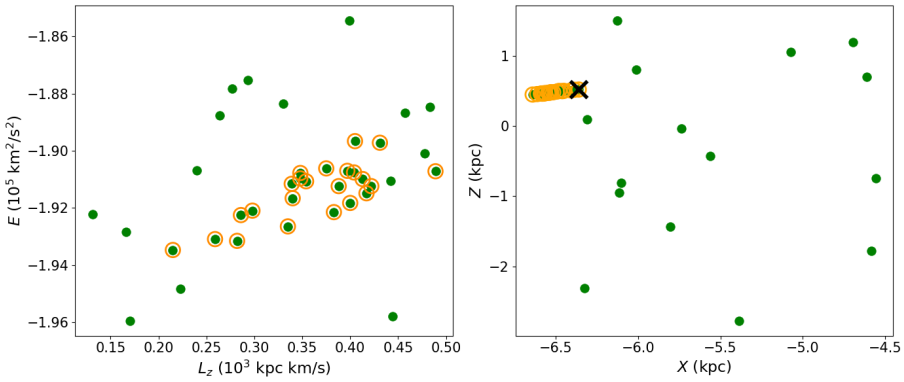

Fig. 10. Distribution of RRLs in Shiva (green dots) shown in the energy versus L_z plane (*left*) and the Cartesian Z versus X plane (*right*). Orange open circles indicate RRLs identified as members of NGC 6121, according to the Clement et al. (2001) catalogue. The black cross identifies the centre of NGC 6121, calculated using coordinates from Baumgardt et al. (2019) and the distance from Baumgardt & Vasiliev (2021).

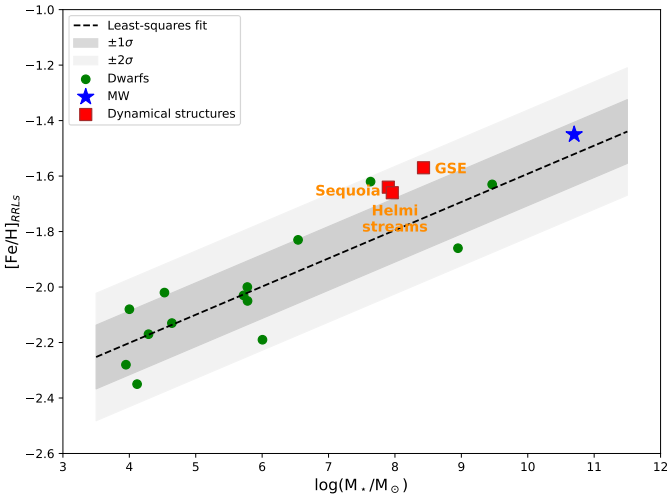

Fig. 11. Mean photometric metallicity of RRLs versus stellar mass for 14 dwarf galaxies (green circles) and the MW (blue star) from Bellazzini et al. (2025), and for the known dynamical sub-structures analysed in this work (red squares). The dashed black line shows the best fit to the 14 dwarfs from Bellazzini et al. (2025), while the dark and light grey areas indicate the $\pm1\sigma$ and $\pm2\sigma$ regions, respectively.

of the MW (Bellazzini et al. 2025), demonstrating that the MZR based on RRLs is a powerful tool for estimating the mass of both existing and accreted satellites of the MW.

The sub-structures identified by CLiMB in correspondence with Shiva and Shakti have the mean metallicities of [Fe/H] = -1.38 ± 0.29 dex and [Fe/H] = -1.41 ± 0.38 dex, respectively. The MZR based on RRLs would yield corresponding progenitor stellar masses of $M_\star = 5 \times 10^{11} M_\odot$ for Shiva and $M_\star = 3 \times 10^{11} M_\odot$ for Shakti, higher than those of the MW, supporting the conclusion that the groups of RRLs identified by CLiMB that we associate to Shiva and Shakti are likely dominated by stars originated in situ, as already discussed in Section 4.10.

Based on the MZR of RRLs and assuming ED-2 is a galaxy, we estimate its approximate mass to be $M_\star = 10^4 M_\odot$ if we consider only the metal-poor star ([Fe/H] = -2.21 ± 0.34 dex), which is in agreement with the findings of Balbinot et al. (2024). If instead we consider the mean metallicity of the two RRLs in ED-2, [Fe/H] = -1.94 ± 0.32 dex, the stellar mass would be $M_\star = 3 \times 10^6, M_\odot$, close to the Thamnos stellar mass (Naidu et al. 2020). However, as discussed in Section 4.8, the more metal-rich RRL in ED-2 is likely a contaminant. Moreover, as discussed in Section 4.8, the progenitor of ED-2 is likely to be the remnant of a GC (Balbinot et al. 2024; Dodd et al. 2025a).

6. Conclusion

We analysed a sample of 4933 RRLs for which accurate coordinates, radial velocities, and proper motions were available from the *Gaia* EDR3 (Gaia Collaboration 2021) and DR3 (Gaia Collaboration 2023b) catalogues, while the geometric distances were estimated from the *Gaia* EDR3 parallaxes using a Bayesian approach (Bailer-Jones et al. 2021). We calculated the IoM (E, L_z, $L_\perp$) as well as the orbital parameters (e.g. apocentre, pericentre, and eccentricity) for all 4933 RRLs in the sample. We then applied the semi-supervised, two-phase CLiMB algorithm (Monti et al. 2026) to identify both previously reported by D23 and newly discovered dynamical sub-structures. In the first phase, CLiMB assigned 630 RRLs to known sub-structures identified by D23, representing a 35% increase in membership compared to their original sample. The second (exploratory) phase successfully identified the extended MW disc structure, as well as two over-densities in correspondence with the newly discovered sub-structures Shiva and Shakti (Malhan & Rix 2024). Photometric metallicities with uncertainties smaller than 0.5 dex were available for 3614 of the 4933 RRLs. We used these metallicities to perform a detailed analysis of identified dynamical sub-structures:

- MW disc: the CLiMB algorithm identified a disc-like structure that contains RRLs originating from the thin disc, thick disc, and HD. Based on their eccentricity and $Z_{\rm max}$, we separated the RRLs in this structure into a thin-disc component, consisting of 238 stars, and a thick-disc component, consisting of 600 RRLs. The two components have mean metallicities of [Fe/H] = -0.75 ± 0.40 dex and [Fe/H] = -1.27 ± 0.42 dex, respectively;
- GSE: the CLiMB algorithm identified 398 RRLs in GSE, 315 of which have accurate metallicity estimates from Muraveva et al. (2025), with a mean metallicity of [Fe/H] = -1.57 ± 0.25 dex. This value is significantly lower than the mean metallicity of GSE overall stellar population (Dodd et al. 2023; Bellazzini et al. 2023). This discrepancy suggests that star formation within the GSE progenitor continued for an extended period following the formation epoch of RRLs, persisting until the GSE structure was accreted by the MW;
- Thamnos: the RRL metallicity distribution in Thamnos was found to be bimodal. The metal-poor peak, likely representing the 'true' Thamnos population, yielded a mean metallicity of [Fe/H] = -1.94 ± 0.20 dex. The metal-rich component ([Fe/H] = -1.35 ± 0.12 dex) is likely contamination from GSE and in situ RRLs;
- Sequoia and Helmi streams: Sequoia RRLs exhibit a mean metallicity of [Fe/H] = -1.64 ± 0.26 dex, while the mean metallicity of RRLs in the Helmi streams is [Fe/H] =

-1.66 ± 0.19 dex. Both sub-structures have mean RRL metallicities that are in good agreement with the values found for the overall stellar population in these sub-structures reported in the literature. This result suggests that, differently from GSE, star formation in these systems halted relatively close to the epoch of RRL formation;
– The mean metallicities of RRLs in ED-1 and L-RL3 are [Fe/H] = -1.57 ± 0.40 dex and [Fe/H] = -1.54 ± 0.33 dex, respectively. Based on their MDFs and their distribution in IoM space, we conclude that both sub-structures likely contain significant contamination from thick disc stars, while the weak metal-poor tails in their MDFs may be signatures of remnants from small accreted systems;
– L-RL64 and ED-2: Due to the small number of RRLs identified in L-RL64 (one star) and ED-2 (two stars with available metallicities), it is difficult to place reliable constraints on their origins. However, the single confirmed extremely metal-poor star in ED-2 ([Fe/H] = -2.21 ± 0.34 dex) supports the hypothesis that it is a remnant of a GC. Meanwhile, we lack sufficient information to determine whether the single RRL discovered in L-RL64, with [Fe/H] = -1.57 ± 0.41 dex, is a true member or a contaminant of an in situ or GSE origin;
– Shiva: The exploratory phase of CLiMB led to the identification of two groups corresponding to the recently reported sub-structures Shiva and Shakti (Malhan & Rix 2024). Our analysis suggests that the over-density of RRLs identified by the CLiMB algorithm in the region of Shiva is primarily due to RRLs belonging to the GC NGC 6121 (M4);
– Shakti: We found that Shakti lies precisely within a known ridge-like structure in the $L_{z,cha}$–E_{cha} plane that originates from resonances with the MW bar. Moreover, we find that 14 out of 58 RRLs in Shakti (24%) are trapped in resonant orbits. Finally, a KS test between the metallicity distributions of Shakti and the thick disc yields a p-value of 0.16, suggesting that the probability that our RRL samples of Shakti and of the thick disc were drawn from the same metallicity distribution is not negligible. We thus conclude that Shakti is likely part of the thick-disc population that became trapped in a resonant feature.

Finally, we used the MZR based on RRLs (Bellazzini et al. 2025) to test the nature of the identified dynamical sub-structures. RRLs are a valuable tool for analysing the MZR at early epochs ($z \gtrsim 3$), close to when the progenitors of present-day dynamical sub-structures merged into the MW. The known accreted sub-structures (i.e. GSE, Sequoia, Helmi streams) were found to lie within 2σ of the best-fit MZR derived from dwarf satellites.

The high metallicities of clusters identified in correspondence with Shiva and Shakti conflict with an accreted origin according to the MZR, confirming their likely in situ origin. Applying the MZR to the confirmed metal-poor RRL in ED-2, we found a progenitor mass of $M_\star \approx 10^4 M_\odot$, consistent with ED-2 having been a very low-mass galaxy. However, the progenitor of ED-2 is likely the remnant of a GC (Balbinot et al. 2024; Dodd et al. 2025a). Overall, this work demonstrates the power of using RRLs to refine our understanding of the origins and compositions of MW halo sub-structures.

A more extensive study of MW dynamical sub-structures, as traced with RRLs, will be enabled by the arrival of *Gaia* Data Release 4 (DR4), currently expected in December 2026. Based on 66 months of observations, *Gaia* DR4 will provide high-cadence light curves and updated Fourier parameters for a vast number of RRLs, which will yield more accurate photometric metallicities, crucial for confirming the nature of ancient structures. Moreover, the accurate astrometric data will be further enhanced by a dramatic increase in radial velocities, delivering the 6D phase-space information required for sophisticated chemo-dynamical analysis of the MW halo. This comprehensive dataset will provide a timely opportunity to refine the CLiMB algorithm by optimising its training sets to reduce contamination between overlapping structures. Together, these observational and algorithmic advancements stand to provide a significant contribution towards reconstructing the MW's assembly history and characterising its earliest building blocks.

Data availability

Full Table A.1 is available at the CDS via anonymous ftp to https://cdsarc.cds.unistra.fr/viz-bin/cat/J/A+A/708/A384

Acknowledgements. We thank the anonymous referee for their thoughtful and constructive review which helped improve the paper. We also thank Dr. Michele Bellazzini and Dr. Emma Dodd for fruitful and interesting discussions which helped improve the manuscript. This work made use of Astropy:[5] a community-developed core Python package and an ecosystem of tools and resources for astronomy (Astropy Collaboration 2013, 2018, 2022). Support to this study has been provided by INAF Mini-Grant (PI: Tatiana Muraveva), by the Agenzia Spaziale Italiana (ASI) through contract ASI 2018-24-HH.0, its Addendum 2018-24-HH.1-2022 and contract ASI 2025-10-H.00, and by Premiale 2015, MIning The Cosmos – Big Data and Innovative. This work uses data from the European Space Agency mission *Gaia* (https://www.cosmos.esa.int/gaia), processed by the *Gaia* Data Processing and Analysis Consortium (DPAC; https://www.cosmos.esa.int/web/gaia/dpac/consortium). Funding for the DPAC has been provided by national institutions, in particular the institutions participating in the *Gaia* Multilateral Agreement.

References

Abolfathi, B., Aguado, D. S., Aguilar, G., et al. 2018, ApJS, 235, 42
Aguado, D. S., Belokurov, V., Myeong, G. C., et al. 2021, ApJ, 908, L8
Amarante, J. A. S., Beraldo e Silva, L., Debattista, V. P., & Smith, M. C. 2020, ApJ, 891, L30
Amarante, J. A. S., Debattista, V. P., Beraldo e Silva, L., Laporte, C. F. P., & Deg, N. 2022, ApJ, 937, 12
Astropy Collaboration (Robitaille, T. P., et al.) 2013, A&A, 558, A33
Astropy Collaboration (Price-Whelan, A. M., et al.) 2018, AJ, 156, 123
Astropy Collaboration (Price-Whelan, A. M., et al.) 2022, ApJ, 935, 167
Bailer-Jones, C. A. L., Rybizki, J., Fouesneau, M., Demleitner, M., & Andrae, R. 2021, AJ, 161, 147
Balbinot, E., Dodd, E., Matsuno, T., et al. 2024, A&A, 687, L3
Baumgardt, H., & Vasiliev, E. 2021, MNRAS, 505, 5957
Baumgardt, H., Hilker, M., Sollima, A., & Bellini, A. 2019, MNRAS, 482, 5138
Bellazzini, M., Massari, D., De Angeli, F., et al. 2023, A&A, 674, A194
Bellazzini, M., Muraveva, T., & Garofalo, A. 2025, A&A, 698, L10
Belokurov, V., & Kravtsov, A. 2022, MNRAS, 514, 689
Belokurov, V., Erkal, D., Evans, N. W., Koposov, S. E., & Deason, A. J. 2018, MNRAS, 478, 611
Belokurov, V., Sanders, J. L., Fattahi, A., et al. 2020, MNRAS, 494, 3880
Belokurov, V., Vasiliev, E., Deason, A. J., et al. 2023, MNRAS, 518, 6200
Beraldo e Silva, L., Debattista, V. P., Nidever, D., Amarante, J. A. S., & Garver, B. 2021, MNRAS, 502, 260
Bobrick, A., Iorio, G., Belokurov, V., et al. 2024, MNRAS, 527, 12196
Bono, G., Caputo, F., Castellani, V., et al. 2003, MNRAS, 344, 1097
Buder, S., Sharma, S., Kos, J., et al. 2021, MNRAS, 506, 150
Buder, S., Lind, K., Ness, M. K., et al. 2022, MNRAS, 510, 2407
Cabrera Garcia, J., Beers, T. C., Huang, Y., et al. 2024, MNRAS, 527, 8973
Catelan, M., Pritzl, B. J., & Smith, H. A. 2004, ApJS, 154, 633
Ceccarelli, E., Massari, D., Mucciarelli, A., et al. 2024, A&A, 684, A37
Ceccarelli, E., Massari, D., Palla, M., et al. 2025, A&A, 704, A180
Clement, C. M., Muzzin, A., Dufton, Q., et al. 2001, AJ, 122, 2587
Clementini, G., Gratton, R., Bragaglia, A., et al. 2003, AJ, 125, 1309
Clementini, G., Ripepi, V., Garofalo, A., et al. 2023, A&A, 674, A18

[5] http://www.astropy.org

Conroy, C., Bonaca, A., Cargile, P., et al. 2019, ApJ, 883, 107
Crestani, J., Fabrizio, M., Braga, V. F., et al. 2021, ApJ, 908, 20
Cui, X.-Q., Zhao, Y.-H., Chu, Y.-Q., et al. 2012, Res. Astron. Astrophys., 12, 1197
Davies, D. L., & Bouldin, D. W. 2009, IEEE Trans. Pattern Anal. Mach. Intell., PAMI-1, 224
Davies, E. Y., Vasiliev, E., Belokurov, V., Evans, N. W., & Dillamore, A. M. 2023, MNRAS, 519, 530
De Leo, M., Massari, D., Bellazzini, M., et al. 2026, A&A, 707, A310
De Silva, G. M., Freeman, K. C., Bland-Hawthorn, J., et al. 2015, MNRAS, 449, 2604
Deepak. 2024, J. Astrophys. Astron., 45, 25
Di Matteo, P., Haywood, M., Lehnert, M. D., et al. 2019, A&A, 632, A4
Dillamore, A. M., Belokurov, V., Evans, N. W., & Davies, E. Y. 2023, MNRAS, 524, 3596
Dodd, E., Callingham, T. M., Helmi, A., et al. 2023, A&A, 670, L2
Dodd, E., Matsuno, T., Helmi, A., et al. 2025a, A&A, 700, A154
Dodd, E., Ruiz-Lara, T., Helmi, A., et al. 2025b, A&A, 698, A277
D'Orazi, V., Storm, N., Casey, A. R., et al. 2024, MNRAS, 531, 137
Gaia Collaboration (Brown, A. G. A., et al.) 2018, A&A, 616, A1
Gaia Collaboration (Brown, A. G. A., et al.) 2021, A&A, 649, A1
Gaia Collaboration (Montegriffo, P., et al.) 2023a, A&A, 674, A33
Gaia Collaboration (Vallenari, A., et al.) 2023b, A&A, 674, A1
Gallart, C., Bernard, E. J., Brook, C. B., et al. 2019, Nat. Astron., 3, 932
Gilligan, C. K., Chaboyer, B., Marengo, M., et al. 2021, MNRAS, 503, 4719
Gómez, F. A., Helmi, A., Cooper, A. P., et al. 2013, MNRAS, 436, 3602
González-Koda, Y. K., Ruiz-Lara, T., Gallart, C., et al. 2025, A&A, 704, A259
GRAVITY Collaboration (Abuter, R., et al.) 2018, A&A, 615, L15
Haywood, M., Di Matteo, P., Lehnert, M. D., et al. 2018, ApJ, 863, 113
Helmi, A. 2020, ARA&A, 58, 205
Helmi, A., & de Zeeuw, P. T. 2000, MNRAS, 319, 657
Helmi, A., White, S. D. M., de Zeeuw, P. T., & Zhao, H. 1999, Nature, 402, 53
Helmi, A., Babusiaux, C., Koppelman, H. H., et al. 2018, Nature, 563, 85
Horta, D., Schiavon, R. P., Mackereth, J. T., et al. 2021, MNRAS, 500, 1385
Horta, D., Schiavon, R. P., Mackereth, J. T., et al. 2023, MNRAS, 520, 5671
Ibata, R. A., Gilmore, G., & Irwin, M. J. 1994, Nature, 370, 194
Johnston, K. V., Hernquist, L., & Bolte, M. 1996, ApJ, 465, 278
Jurcsik, J., & Kovacs, G. 1996, A&A, 312, 111
Kepley, A. A., Morrison, H. L., Helmi, A., et al. 2007, AJ, 134, 1579
Koppelman, H., Helmi, A., & Veljanoski, J. 2018, ApJ, 860, L11
Koppelman, H. H., Helmi, A., Massari, D., Price-Whelan, A. M., & Starkenburg, T. K. 2019a, A&A, 631, L9
Koppelman, H. H., Helmi, A., Massari, D., Roelenga, S., & Bastian, U. 2019b, A&A, 625, A5
Koppelman, H. H., Bos, R. O. Y., & Helmi, A. 2020, A&A, 642, L18
Kruijssen, J. M. D., Pfeffer, J. L., Chevance, M., et al. 2020, MNRAS, 498, 2472
Kunder, A., Rich, R. M., Koch, A., et al. 2016, ApJ, 821, L25
Kunder, A., Kordopatis, G., Steinmetz, M., et al. 2017, AJ, 153, 75
Kunder, A., Pérez-Villegas, A., Rich, R. M., et al. 2020, AJ, 159, 270
Kunder, A., Prudil, Z., Skaggs, C., et al. 2024, AJ, 168, 139
Lane, J. M. M., Bovy, J., & Mackereth, J. T. 2023, MNRAS, 526, 1209
Li, X.-Y., Huang, Y., Liu, G.-C., Beers, T. C., & Zhang, H.-W. 2023, ApJ, 944, 88
Liu, G. C., Huang, Y., Zhang, H. W., et al. 2020, ApJS, 247, 68
Longmore, A. J., Fernley, J. A., & Jameson, R. F. 1986, MNRAS, 220, 279
Lövdal, S. S., Ruiz-Lara, T., Koppelman, H. H., et al. 2022, A&A, 665, A57
Malhan, K., & Rix, H.-W. 2024, ApJ, 964, 104
Massari, D., Koppelman, H. H., & Helmi, A. 2019, A&A, 630, L4
Matsuno, T., Aoki, W., & Suda, T. 2019, ApJ, 874, L35
Matsuno, T., Koppelman, H. H., Helmi, A., et al. 2022, A&A, 661, A103
McMillan, P. J. 2017, MNRAS, 465, 76
Monty, S., Venn, K. A., Lane, J. M. M., Lokhorst, D., & Yong, D. 2020, MNRAS, 497, 1236
Monti, L., Muraveva, T., Sheridan, B., et al. 2026, arXiv e-prints [arXiv:2601.09768]
Moreno, E., Pichardo, B., & Schuster, W. J. 2015, MNRAS, 451, 705
Moreno, E., Fernández-Trincado, J. G., Schuster, W. J., Pérez-Villegas, A., & Chaves-Velasquez, L. 2021, MNRAS, 506, 4687
Morgan, S. M., Wahl, J. N., & Wieckhorst, R. M. 2007, MNRAS, 374, 1421
Mori, A., Di Matteo, P., Salvadori, S., et al. 2024, A&A, 690, A136
Mori, A., Di Matteo, P., Salvadori, S., et al. 2025, A&A, submitted, [arXiv:2509.13408]
Muraveva, T., Delgado, H. E., Clementini, G., Sarro, L. M., & Garofalo, A. 2018, MNRAS, 481, 1195
Muraveva, T., Giannetti, A., Clementini, G., Garofalo, A., & Monti, L. 2025, MNRAS, 536, 2749
Myeong, G. C., Evans, N. W., Belokurov, V., Sanders, J. L., & Koposov, S. E. 2018, ApJ, 863, L28
Myeong, G. C., Vasiliev, E., Iorio, G., Evans, N. W., & Belokurov, V. 2019, MNRAS, 488, 1235
Naidu, R. P., Conroy, C., Bonaca, A., et al. 2020, ApJ, 901, 48
Nepal, S., Chiappini, C., Queiroz, A. B., et al. 2024, A&A, 688, A167
Oria, P.-A., Tenachi, W., Ibata, R., et al. 2022, ApJ, 936, L3
Pace, A. B. 2025, Open J. Astrophys., 8, 142
Rey, M. P., Agertz, O., Starkenburg, T. K., et al. 2023, MNRAS, 521, 995
Ruiz-Lara, T., Matsuno, T., Lövdal, S. S., et al. 2022, A&A, 665, A58
Sarbadhicary, S. K., Heiger, M., Badenes, C., et al. 2021, ApJ, 912, 140
Skúladóttir, Á., Ernandes, H., Feuillet, D. K., et al. 2025, ApJ, 986, L21
Sollima, A., Cacciari, C., Arkharov, A. A. H., et al. 2008, MNRAS, 384, 1583
Soszyński, I., Udalski, A., Szymański, M. K., et al. 2014, Acta Astron., 64, 177
Soszyński, I., Udalski, A., Wrona, M., et al. 2019, Acta Astron., 69, 321
Sun, S., Wang, F., Zhang, H., et al. 2025, ApJ, 979, 213
Tenachi, W., Oria, P.-A., Ibata, R., et al. 2022, ApJ, 935, L22
Thomas, G. F., Battaglia, G., Grand, R. J. J., & Aguiar Álvarez, A. 2025, A&A, 704, A40
Tononi, J., Torres, S., García-Berro, E., et al. 2019, A&A, 628, A52
Vasiliev, E. 2019, MNRAS, 482, 1525
Vincenzo, F., Spitoni, E., Calura, F., et al. 2019, MNRAS, 487, L47
White, S. D. M., & Frenk, C. S. 1991, ApJ, 379, 52

Appendix A: Dataset

Table A.1. Parameters of the 4933 RRLs in the reference sample.

source_id	RA	Dec.	pmra	pmdec	L_z	E	$L_\perp$	ecc	[Fe/H]	$\sigma_{[Fe/H]}$	Substructure
5930541561668628736	249.1970	-54.2037	-17.171	-14.857	-745	-177885	344	0.59	-2.11	0.42	Thamnos
6471410229148825088	310.1242	-53.2819	-7.662	-28.896	-1789	-133202	821	0.56	-1.75	0.42	Sequoia
34113623857898880	44.5915	15.6717	1.760	-37.565	98	-135829	26	0.98	-1.64	0.44	GSE
1193183528770580224	238.6171	15.3561	-17.853	1.871	-252	-154345	210	0.91	-1.49	0.44	GSE
1196737700107586176	238.3152	17.5699	-11.729	-4.870	-533	-179584	361	0.59	-1.88	0.41	Thamnos
2098060604631085952	279.6238	39.5011	-1.520	-5.618	291	-180257	503	0.84	-1.65	0.35	L-RL3
5768557209320424320	248.1040	-83.9035	-58.488	-120.550	-218	-160786	789	0.91	-1.97	0.50	GSE
702294777158642688	139.9645	33.8732	-3.352	-12.630	226	-160275	272	0.87	-1.50	0.41	GSE
2538463596221422976	18.4185	2.1610	7.466	-11.608	-262	-167128	211	0.85	-1.30	0.35	GSE
5783102618581820672	192.5538	-81.9544	9.371	1.509	-64	-140426	722	0.95	-1.63	0.40	GSE

Notes. Column (1) *Gaia* DR3 `source_id`; (2) and (3) Coordinates; (4) and (5) Proper motions; (6) Angular momentum along the Z-axis; (7) Total energy; (8) Component of angular momentum perpendicular to L_z; (9) Eccentricity; (10) and (11) Photometric metallicities and their corresponding uncertainties; (12) The sub-structure to which the star is assigned by the CLiMB algorithm.
Columns (1)–(5) are taken from the *Gaia* DR3 `gaia_source` table (Gaia Collaboration 2023b). Columns (6)–(9) and (12) are calculated in this study. Columns (10) and (11) are from Muraveva et al. (2025). The full table is published at the CDS; a portion is shown here to illustrate its form and content.